Dinesh Ram, B.Tech

Effect of thermal treatment parameters on the age-hardening of AlSi7Cu0.5Mg

MASTER'S THESIS

to achieve the university degree of

Diplom-Ingenieur

Master's degree programme: Advanced Materials Science

submitted to

Graz University of Technology

Supervisor

Assoc.Prof. Dr.techn., Maria Cecilia Poletti

Co-Supervisor
Dipl.-Ing,René Wang, B.Sc

3030 Institute of Materials Science, Joining and Forming

Graz, May 2019

AFFIDAVIT

I declare that I have authored this thesis independently, that I have not used other than the declared sources/resources, and that I have explicitly indicated all material which has been quoted either literally or by content from the sources used. The text document uploaded to TUGRAZonline is identical to the present master's thesis.

17.05.2019

Date

Signature

Acknowledgements

Firstly, I would like to thank Dipl.-Ing. R. Wang who warmly welcomed me to the Institute of Materials Science, Joining and Forming, and being a constant pillar of support and supervision with his knowledge throughout the work. Likewise, enormous thanks to Assoc.-Prof. Dr.techn. M. C. Poletti for the supervision and insightful suggestions. Both of them being instrumental in completing my thesis.

Acknowledging project partners Christian Doppler-Laboratory for Design of High-Performance Alloys by Thermomechanical Processing and Nemak Linz GmbH and in particular Dr.techn. R. Fernandez Gutierrez and Dr.mont. B. Stauder for their vote of confidence.

Also, would like to thank all IMAT scientific staff in particular Dipl.-Ing. Dr. mont. F. Krumphals and Eng. Mestr. R.H. Buzolin for their practical suggestions. Immensely thankful to the laboratory staff Ing. H. Penker, Ing. K. Kerschbaumer, G. Stöfan and T. Friedl for giving valuable training and technical support for the equipment at the institute.

Thanks to Mag. Dr.rer.nat. R. Nuster and Assoc.-Prof. Dipl.-Ing. Dr.techn. G. Trimmel for the collaboration.

Special thanks to my friends, especially my roommates Keerthi and Yashas for their cordial feedbacks.

Last but not the least, thankful to my family who made this possible for me and more than above for their unconditional love.

Dinesh Ram

Table of Contents

List of abbreviation

AA: Aluminum Association
BSE: Backscattered electrons signal
CW: Continuous Wave
DIL: Dilatometry
DSC: Differential Scanning Calorimetry
E: Young's modulus of elasticity
EDX: Energy Dispersive X-Ray elemental mapping
HV: Vickers Hardness Number
LOM: Light Optical Microscopy
LUS: Laser induced Ultrasound
SAWs: Surface Acoustic Waves
SC: specimen current
SEM: Scanning Electron Microscopy
SEs: secondary electrons
SHT: Solution Heat Treatment
TEM: Transmission Electron Microscopy
ρ: Mass density

Abstract

Al cast alloys are being increasingly used, particularly in automobile, aerospace and sports industries [1]. To optimise, augment and adapt the mechanical properties for a specific application, the alloys are thermally treated, and it is critical to determine the influencing parameters and their effects. Parameters of the heat treatment process of AlSi7MgCu0.5, like quenching rate, aging time and temperature, have been systematically investigated. The alloy has been artificially and naturally aged in different quenching rates. Subsequently the hardness within the Al- matrix has been measured by Vickers micro hardness testing. Further characterisations were done, using Scanning Electron Microscopy (SEM) and Energy Dispersive X-Ray (EDX) elemental mapping Laser induced Ultrasound (LUS) technique [2], Differential Scanning Calorimetry (DSC) and in-situ isothermal dilatometry. The work attempts to portray the results of above microstructural characterisations and their implications on the precipitation sequence of phases formed during ageing and mechanical properties. The hardness is found to increase with increasing aging time up to peak age condition and with increasing aging temperature a shorter time to achieve peak age. A significant drop in hardness is found at higher aging temperature of 230 °C and at lower quenching rates (< 2 K/s). The first aspect is the indication of coarsening of precipitates, while the second aspect is related to the clustering occurring already during slow cooling rate, in detriment of the aging potential for subsequent aging step. DSC characterisation has been employed to identify the precipitation state of some relevant samples. Dilatometry has been found to be unique and important in-situ technique to identify isothermal transformations.

Keywords: Al-Si-Cu-Mg alloys, age hardening, precipitation hardening, Vickers micro-hardness testing, SEM, EDS, Laser induced Ultrasound (LUS)characterisation, Dilatometry.

Kurzfassung

Durch thermische Behandlung von Al-Gusslegierungen können gewünschte mechanische Eigenschaften passend zur Anwendung erreicht werden. Daher ist es erforderlich die Prozessparameter von Wärmebehandlungen, sowie deren Einfluss auf die Mikrostruktur und auf die mechanischen Eigenschaften zu bestimmen. In dieser Arbeit wurden essenzielle Parameter des Wärmebehandlungsprozesses von AlSi7MgCu0.5, wie Abkühlgeschwindigkeit nach dem Lösungsglühen, Auslagerungszeit und -temperatur systematisch untersucht. Die Legierung wurde lösungsgeglüht und mit verschiedenen Abkühlgeschwindigkeiten abgeschreckt, darauffolgend warm- bzw. kaltausgelagert und die Härte durch Messung der Vickers-Mikrohärte in der Al-Matrix bestimmt. Neben Härtemessungen wurde das Gefüge auch mittels Rasterelektronenmikroskopie (REM), energiedispersive Röntgenspektroskopie (EDRS), LUS, dynamischer Differenzkalorimetrie (DDK) und isothermer Dilatometrieanalyse charakterisiert. Der Einfluss der Prozessparameter auf die Härte der Legierung wurde dann dargestellt. Die Ergebnisse zeigen, dass die Härtewerte mit voranschreitender Auslagerungszeit eine Maximalhärte erreichen und diese Maximalhärte bei höheren Auslagerungstemperaturen früher erreicht wird. Mit weiter voranschreitender Auslagerungszeit nimmt die Härte wieder ab. Ein signifikanter Härterückgang konnte bei niedrigen Abkühlgeschwindigkeiten beim Abschrecken (< 2 K/s) kombiniert mit hohen Auslagerungstemperaturen (230 °C) beobachtet werden. Dieser Effekt ist einerseits ein Hinweis auf die Vergröberung von Ausscheidungen und zeigt andererseits bereits während des langsamen Abkühlens eine einsetzende Clusterbildung von Ausscheidungen, welche sich negativ auf das Auslagerungspotential für den nachfolgenden Auslagerungsprozess auswirkt. Zur Identifizierung des Ausscheidungszustands wurde für ausgewählte Proben eine DDK-Analyse, sowie in-situ Dilatometrie durchgeführt.

Schlagwörter: Al-Si-Mg-Cu-Legierung, Ausscheidungsshärtung, Vickers-Mikrohärte-Messung, REM, EDRS, LUS, DDK, Dilatometrie.

1. Introduction

1.1. Motivation

Aluminium is one of the most widely used and produced metal after steel. Aluminium is used in major areas: building and construction; containers and packaging; automobiles; electrical conductors; machinery and equipment. The largest potential for growth in use of aluminium is in automotive sector. Major classification of aluminium alloys is wrought and cast alloys. Even though wrought alloys constitute the most of aluminium produced, cast alloys are being increasingly used, particularly in automobile industry. The most widely used cast alloys are based on Al-Si, Al-Si-Cu and Al-Si-Mg systems. [1]

The present work investigates the AlSi7MgCu0.5-alloy, used for cylinder heads in the automotive industry.

These alloys are usually heat treated for their application to develop adequate strength and hardness. The heat treatment involves solution heat treatment, quenching to room temperature and aging at a particular temperature.

To optimise and adapt the heat treatment, it is important to determine the influence of parameters, like ageing temperature, time and cooling rate on mechanical properties.

1.2. Objectives

The objective of this work is to determine the influence of ageing temperature, time and cooling rate from solution heat treatment on the precipitation sequence and mechanical properties. To achieve the main objective, it is classified into following:

- Influence of the ageing temperature, time and quenching rate on the hardness using Vickers micro-hardness testing.
- Influence of the quenching rate on the isothermal length change and heat flow studies of the specimens using dilatometry and Differential Scanning Calorimetry (DSC) respectively.
- Influence of the quenching rate on the precipitation states, visualised through Scanning Electron Microscopy (SEM) and Energy Dispersive X-Ray elemental mapping (EDX).

- Characterisation of age hardening using Laser induced Ultrasound Spectroscopy (LUS).

2. State of the art

This chapter includes the general information about Al-alloys and then describes different phases in the precipitation sequence of Al-Si alloy systems. It also comprises the different heat treatments routinely used in Al-Si cast alloys, principles of precipitation hardening and different microstructural characterisations.

Aluminum is a versatile of the common foundry metals. For light weight design, the good stiffness in bending ($\sqrt{E}/\rho$) is the main advantage of aluminum alloys compared to steels. The high stiffness module makes them attractive for aerospace applications. Another advantage is the relatively low melting temperature compared to other cast materials, making the casting less energy intensive. Further advantage of Al-cast alloys in processing is the insolubility of almost all gases except hydrogen. [1]

One of the drawbacks of aluminum castings is their high volumetric shrinkage during solidification. This must be omitted by the designing of molds in order to achieve dimensional accuracy and to minimize casting defects like hot tearing, residual stresses and shrinkage porosity. [1]

2.1. Classifications and Designations

Al-alloys are classified according to the United States Aluminum Association systems (AA) into two categories: wrought and cast alloys. [1]

Figure 1 shows widely used Al-alloys and their capability to be hardened for applications.

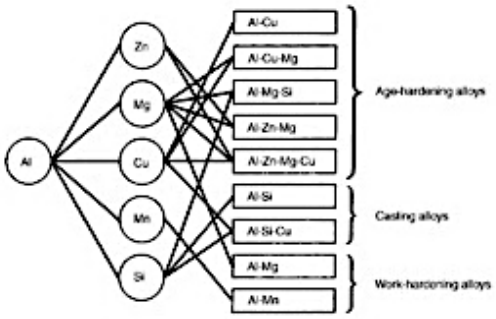

Figure 1: Common Al-alloy systems. [1]

The designations for Al cast alloys are described by a 3-digit system trailed by a decimal value. Table 1 shows AA system designation for Al cast alloys, in which the first digit designates the alloy group and the following digits define the minimum percentage of aluminum content. The product form is indicated by the last digit on the right of the decimal point, .0 for castings and .1 for ingots. [1]

Table 1: Designation for Al cast alloys. [1]

	Current designation
Aluminium, 99.00% or greater	1xx.x
Aluminium alloys grouped by major alloying elements:	
Copper	2xx.x
Silicon with added copper and/or magnesium	3xx.x
Silicon	4xx.x
Magnesium	5xx.x
Zinc	7xx.x
Tin	8xx.x
Other element	9xx.x
Unused series	6xx.x

2.2. General Characteristics

The characteristics required for a cast Al-alloy are summarized in Table 2. The table is organized with description of different characteristics, identified influencing parameter and their influence and the cause of this influence. Fluidity, volumetric shrinkage, porosity, hot tearing and die soldering are the important characteristics that determine the cast-ability of an Al-alloy.

Table 2: Characteristics important for cast-ability of Al-alloys. [1]

Characteristics	**Influencing Parameter**	**Influence**	**Cause**
Fluidity: Ability to flow	Composition	Decreases with increasing the purity of Al	Widening of the freezing range due to formation of intermetallic compounds and change in

			solidification pattern
Volumetric shrinkage: Decrease in volume during solidification	Composition, mold design, cooling rate and mode of solidification	Alloying helps reducing shrinkage. E.g.: Hypereutectic Al-Si	Due to different densities of the liquid/ solid phases
Porosity: Presence of open or closed pores in the bulk	Operating conditions like: Operation speed, turbulent metal flow etc.	Variable influence	Shrinkage, formation of internal oxides and entrapment
Hot tearing	Composition	Al-Mg alloys show hot tearing, Al-Si have good hot tearing resistance.	Tensile stresses generated during solidification exceeds the ultimate tensile stress of partially solidified metal
Die Soldering: tendency in pressure die castings of Al alloys to stick to the ferrous dies.	1. Alloy composition 2. Die Steel Composition 3. Melt injection temperature 4. Surface coating	1. Addition of Fe, Ti has beneficial effects on reducing soldering, unlike Ni. 2. Higher alloyed steels are better, but seldom used. 3. Higher temperatures promote soldering. 4. Coatings minimize soldering.	Affinity of molten Al with Fe. Rapid diffusion promotes intermetallic compound formation

2.3. Alloying Elements and their Influence

Al-Si cast are of particular importance in automotive industries. The advantages include:

- High fluidity
- High stiffness modulus $\sqrt{E}/\rho$ and $\sqrt[3]{E}/\rho$ (E is the Young's modulus of elasticity and ρ is the mass density)
- Good corrosion resistance
- Low expansion coefficient
- Reduced casting shrinkage
- Excellent weld-ability and cast-ability.[1][3]

However, they pose certain difficulties in

- Machinability
- Fracture toughness and ductility
- Origin and propagation of cracks by hard silicon particles.[4]

The eutectic reaction involved in Al-Si system is: $L \rightarrow \alpha(Al) + \beta\ (Si)$

The alloy system has a eutectic point at 12.6 wt.% SI at 577°C, at which the maximum solubility of Si occurs: 1.5 wt.% Si. The eutectic plateau is strongly dependent on cooling rate. The T_0 curve, locus of all points where liquid and solid phase co-exist, and metastable extensions depicted this dependence. Refer to Figure 2. [3]

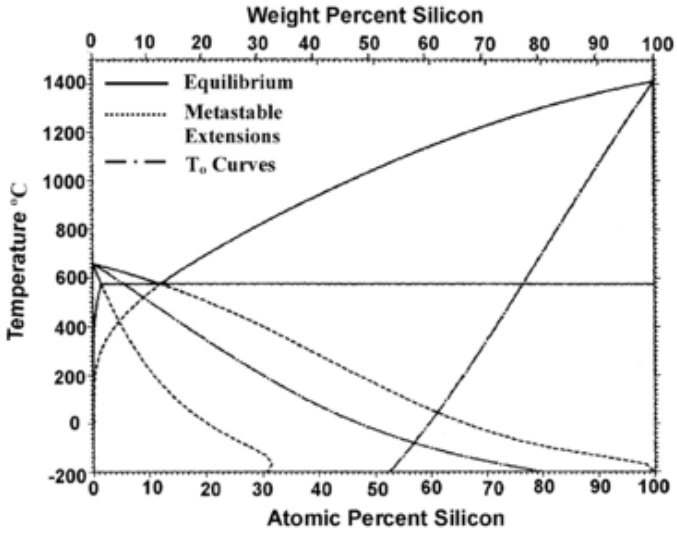

Figure 2: Al-Si Phase diagram with equilibrium states and metastable extensions of the solidus and liquidus line.[3]

The final microstructure is influenced by the cooling rate, as illustrated in Figure 3. The microstructure could of lamellar/fibrous and regular/irregular based on the volume fraction of both phases.[3]

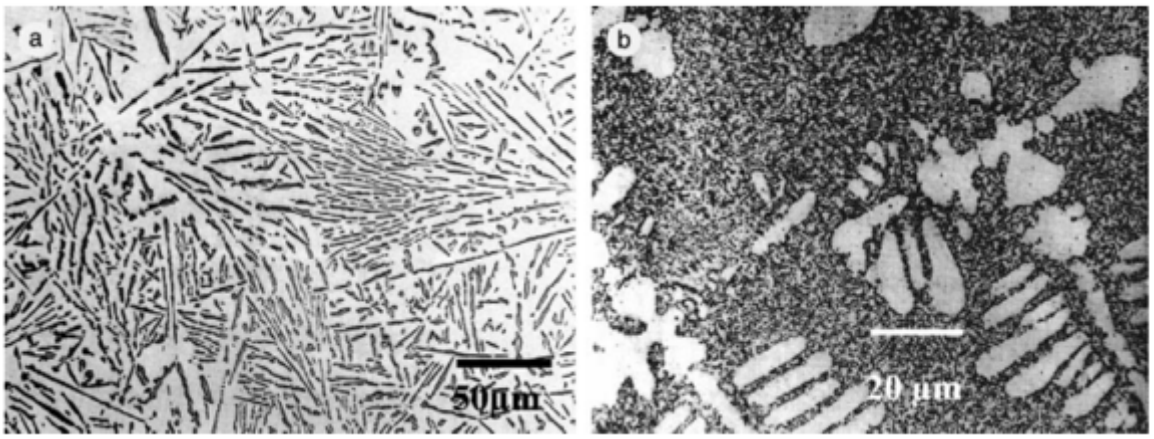

(a) (b)

Figure 3: a. Slowly cooled and b. Chill cast Al-12.5wt.% Si alloy. The bright phase is Al and the dark phase is eutectic Si.[3]

Only a few metals have sufficient solubility in aluminum to be reckoned as major alloying element. The common ones with substantial solubilities are zinc, magnesium (maximum solubility greater than 10 weight %), copper and silicon. (Figure 4) Maximum solubility is obtained at eutectic temperature for all elements except for Cr, Ti, V, Zn and Zr, for which it is obtained at the peritectic temperature.[1]

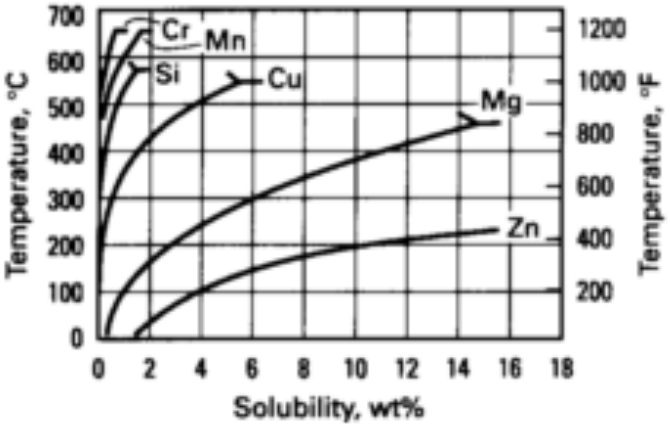

Figure 4: Solubility of common alloying elements in Al-alloy system.[5]

Different alloy elements were identified, and their effect of the alloy system was asserted with reference to the literature. Each alloy element confers changes in

the alloy properties. The maximum composition of the alloying element is also identified. The characteristics that the alloying element brings are also remarked in the following table (Table 3).

Table 3: Influence of various alloying elements in Al-Si alloy system.

Alloying Element	**Influence**	**Max. composition. limited by**	**Remarks**
Mg	Induce age hardening and solid solution hardening. [6]	Formation of phases like π-phase ($Al_8FeMg_3Si_6$) in high Mg, reduce the ductility and fracture, toughness. 0.35-0.45 %.[6]	Precipitation of $MgSi_2$ particles by lowering the eutectic temperature.[6]
Cu	Improve strength and improve the machinability and induce age hardening. [1]	Reduces the cast-ability, ductility and corrosion resistance. 0.40- 0.60 % [1]	The hardness increase is because of precipitation of metastable phases (Q-$Al_4Cu_2Mg_8Si_6$, Θ' – Al_2(Al, Cu), Θ'' – Al_3Cu). [7][8]
Fe	Detrimental to cast-ability, cast-porosity and other mechanical properties. [9]–[11]	Unavoidable impurity induced from recycling processing. (< 0.20 %) [9]–[11]	Formation of coarse β-Al_5FeSi intermetallics. They are crack and pore initiators. [9]–[11]
Mn	Improves tensile properties. [12]	<0.10 %.[12]	Modifies the needle shaped β-Al_5FeSi into dendritic α-Al (Fe, Mn) Si phases. [13]
Ti	Acts as grain refiner.[14]	0.2- 1.0 %.[14]	$TiAl_3$ promotes the nucleation of α-Al at these phases, giving grain refinement. [14]
B	Acts as grain refiner. [14]	<0.03%. [14]	TiB_2 phase also promotes heterogeneous nucleation. [14]

2.4. Precipitation sequence and Heat Treatments

A binary Al-Si alloy can be classified into 3 categories based on the composition of Si: Hypoeutectic (<12.6 wt.%), eutectic (12.6 wt.%) and hypereutectic (>12.6 wt.%) alloys.
In hypoeutectic alloys, the equilibrium phases present are the soft and ductile primary Al phase and hard and brittle eutectic Si. With increase in composition of Si, the eutectic Al-Si phase nucleate and grow till the end of solidification. Further increase of Si into hypereutectic regimes, primary Al, angular primary Si particles and eutectic Si phases are obtained.[3]

2.4.1. Precipitation phases

In the case of Al-Si alloys containing elements like Mg, Cu and Fe, different stable and metastable phases are formed. The type of the phases formed depend on the alloy composition and its thermal history.[15]

The sequence of precipitation is illustrated in Figure 5.

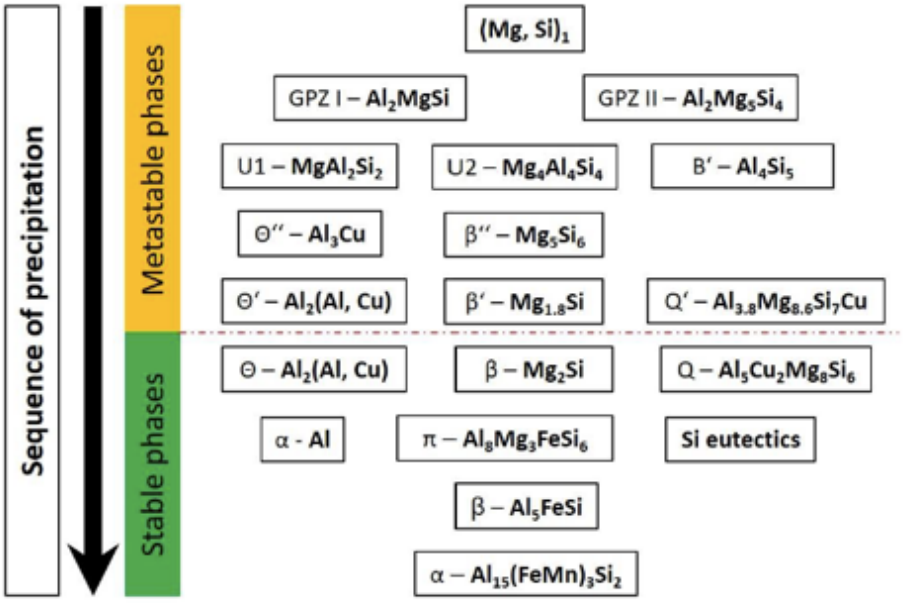

Figure 5: Sequence of precipitation. Adapted from [16].

The precipitation sequence follows in the way that meta-stable phases appear

during quenching and in the early stages of aging and transform into more thermodynamically stable phases with time. [15]

Table 4 summarizes the different thermodynamically less stable (meta-stable) phases and their characteristics.

Table 4: Meta-stable phases and their characteristics.

Phase	**Characteristics**
Atomic clusters- (Mg, Si)	Formed in a very early stage of the aging process: Si, Mg, Cu clusters and co-clusters of Mg, Si later on. [17]
GP(I)- Al_2MgSi and GP(II)- $Al_2Mg_5Si_4$	Formed out of atomic clusters in early stages of aging. GP(I)- spherical, GP(II)-needle-like, both coherent. [17]
U1-$MgAl_2Si_2$	Similar morphology (appear as large needles along <100> direction) than other phases. Of importance due to its high silicon content, but little/no contribution to hardening. [18]
U2- $Mg_2Al_4Si_4$	Orthorhombic, needle-like, <100> aligned, co-exist with β'' and β'. [18]
B'- $Mg_2Al_4Si_5$	Lath-shaped, rectangular cross-section, <100> aligned and hexagonal/base centered orthorhombic. [17]
β''- Mg_5Si_6	Formed out of GP-zones. Monoclinic/hexagonal, needle-shaped, <100> aligned. [17]
β'- $Mg_{1.8}Si$	Transformed from β''. Rod shaped, <100> aligned. Hexagonal crystal structure. [17]
θ''- Al_3Cu	Formed after dissolution of Cu- GP-zones at higher temperature. [19]
θ'- $Al_2(Al, Cu)$	Rectangular/ octagonal plates with body-centered tetragonal structure. Transformed from θ'' upon peak aging, partially coherent with matrix, important in hardening process. [19]
Q'- $Al_3Mg_9Si_7Cu_2$.[20]	Lath/rod shaped hexagonal structure. It is of great importance in the age hardening process. [21]

Table 5 illustrates the different thermodynamically stable phases and their characteristics.

Table 5: Stable phases and their characteristics.

Phase	**Characteristics**
Q-$Al_{4,5}Cu_{1,2}Mg_{5,8}Si_{4,6,7}$	Formed during age hardening. Lath/rod shaped hexagonal structure. Q' meta-stable version of Q is of importance in hardening. The exact stoichiometry of Q and Q' can vary. [21]
θ- Al_2(Al, Cu)	Body-centered tetragonal structure. Of particular importance for hardening. $Al_{SSS} \rightarrow$ Clusters $\rightarrow$ GP-zones $\rightarrow$ θ"$\rightarrow$ θ' $\rightarrow$ θ . [19]
β- Mg_2Si	Face-centered anti-fluorite structure. $Al_{SSS} \rightarrow$ Clusters (Si, Mg) $\rightarrow$ Dissolution of Mg Clusters $\rightarrow$ Co-Clusters (Si, Mg)$\rightarrow$ β" $\rightarrow$ β- Mg_2Si. Important in hardening process. [17]
Intermetallic phases with Fe	Usually monoclinic. E.g. β- $Al_5Mg_3FeSi_6$. Generally detrimental to mechanical properties as they act as stress concentrators. Addition of Mn is adopted to neutralize the effect by forming α- Al (Fe, Mn) Si which has a compact structure.[22]

2.4.2. Heat treatments in cast Al-Si-Cu-Mg alloys

Heat treatments are typically applied to Al-Si-Cu-Mg cast alloys. The heat treatment consists of three steps [23]:

1) Solution heat treatment

The objectives of the solution heat treatments are:

- Dissolution of phases into elements which become later available for precipitation.
- Homogenize the chemical composition.
- Transform β- Al_5FeSi into α- Al (Fe, Mn) Si.
- Spheroidize the eutectic Si phase.

The controlling factors of these process are the solution treatment temperature. The higher the temperature, the higher the rate of the processes. The maximum solution treatment temperature depends on the concentration of Mg and Cu, as dissolution of their phases are important for full aging potential. The exact temperature depends on the solidification temperature and heating rate of solution treatment.[23]

Dissolution

It is the process on dissolving the alloying elements into solid Al matrix.

It is important that the Mg and Cu containing phases dissolve even if it is not possible to dissolve all phases like the Fe-intermetallics: β- Al_5FeSi and α- Al (Fe, Mn) Si. If Cu and Mg atoms that are bound to phases do not dissolve during solution treatment, they will not be available to increase the strength by precipitation hardening.[23]

θ- Al_2(Al, Cu), Q- $Al_{4,5}Cu_{1,2}Mg_{5,8}Si_{4,6,7}$ and β- Mg_2Si are easier to dissolve unlike Fe containing phases, which don't dissolve. The temperature and holding time during solution heat treatment are adequately chosen to get around this issue.

Homogenization

Homogenization refers to atoms detaching from large agglomerations formed during solidification and diffusing into the matrix, forming a homogenous alloy system. The rate of homogenization depends on [23]:

- Type of diffusing atoms.
- Treatment temperature.
- Chemical nature of the matrix.
- Grain size.

Spheroidizing

One of the objectives of solution treatment is to spheroidize large brittle flakes of eutectic Si. The spheroidization rate depends again on the solution treatment temperature and on the morphology and size of Si particles.[23]

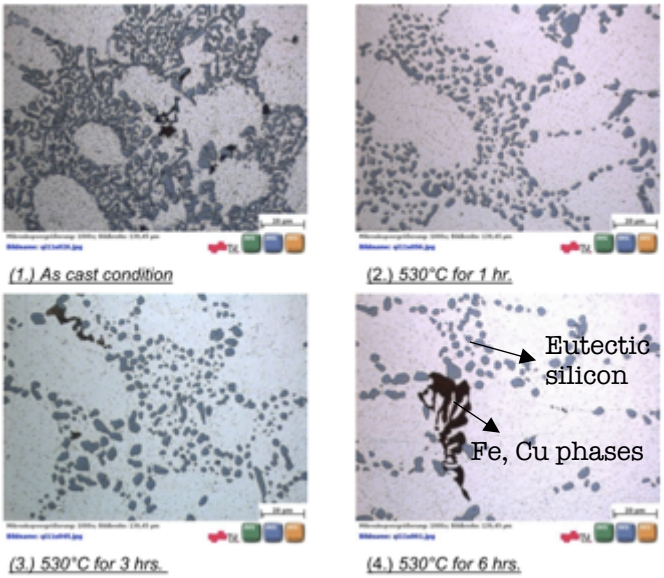

Figure 6: Spheroidization and dissolution of eutectic silicon in G-AlSi7MgCu0.5 alloy over time. (1), (2), (3), (4) represent the as-cast, 1hr., 3hrs.,6hrs. of SHT at 530 °C respectively.

2) Quenching

Quenching is a rapid cooling process, using quenching media like water, oil, air or other gases, etc. The objective of such a process is to prevent spontaneous heterogeneous precipitation during cooling from solution treatment temperature to room temperature. Heterogeneous nucleation occurs at grain boundaries and dislocations, leading to reduction in maximum strength. Therefore, the rate of the process should be high enough to hold the solute and vacancies in the matrix. Figure 7 shows the effects of aging on strengthening and elongation to fracture.[23]

The precipitation progresses through nucleation and growth of precipitates. The highest nucleation and growth rates of precipitates takes place between 200°C to 450°C. Therefore, the time spent for the cooling range in this temperature must be as small as possible. However, a too high cooling rate can cause undesired thermal stresses on the product.[23]

The commonly used medium is water, but for lower cooling rates oil, salt baths and organic solutions can be used. [23]

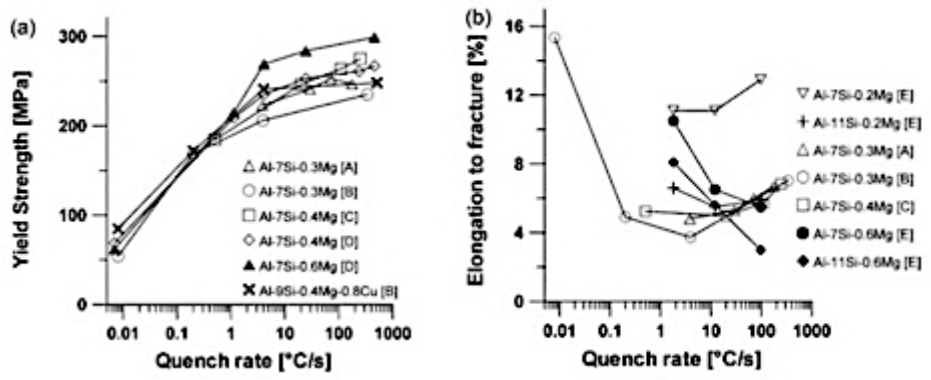

(a) (b)

Figure 7: (a) Yield strength and (b) elongation to fracture for T6 treated Al-Si alloys with different compositions as a function of the quenching rates. [24]

3) Age Hardening

Aging is the process of strengthening the alloy by homogenous distribution of small precipitates in the matrix using room or elevated temperatures for the treatment. Based on the temperature, they can be classified as artificial and natural aging. (Usually 150 °C -230 °C for Al-Si alloys in case of artificial aging, room temperature in case of natural aging).

During aging GP zones form soon after quenching, the supersaturation of solute and high vacancy concentration being the driving force. In the case of natural aging, because of limited diffusion at room temperature, GP zones are small, coherent and finely dispersed. This results in a small critical precipitation radius. In the case of artificial aging the formed precipitates are larger in size.[23]

Figure 8 shows the result of an artificial aging experiment by P. Gumpl [16]. The decrease in hardness after some time (over-aging) is evident. This can be explained by the hardening mechanism illustrated in Figure 8.

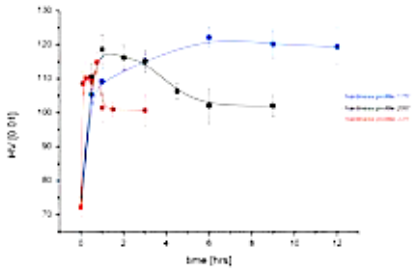

Figure 8: Plot between hardness number and aging time. Artificial aging of G-AlSi7MgCu0.5 alloy done at temperature 175°C, 200°C, 225°C. Taken from [16].

2.5. Precipitation hardening mechanism

The strengthening of the alloy works by retarding dislocation motion due to the presence of secondary phases. The size and distribution of the precipitates and their coherency with respect to the matrix are the most important factors. Small and not so hard precipitates are normally sheared by moving dislocations (Friedel effect) (see Figure 9a)When the precipitates are larger and harder, the moving dislocations must bypass the precipitates by bowing (Orowan mechanism) (see Figure 9b). The strength of the precipitates increases with their size up to a critical size. Thus, growth and coarsening stages are important in hardening; the coarsening leads to larger sized particles, giving way to Orowan mechanism. Further increase of precipitate size, under constant volume fraction of particles follows the Orowan mechanism leading to a decrease in strength (see Figure 9c), when the particles are coarsened. The highest strength is obtained at the critical radius when both Orowan's and Friedel's mechanism equally dominate.[25]

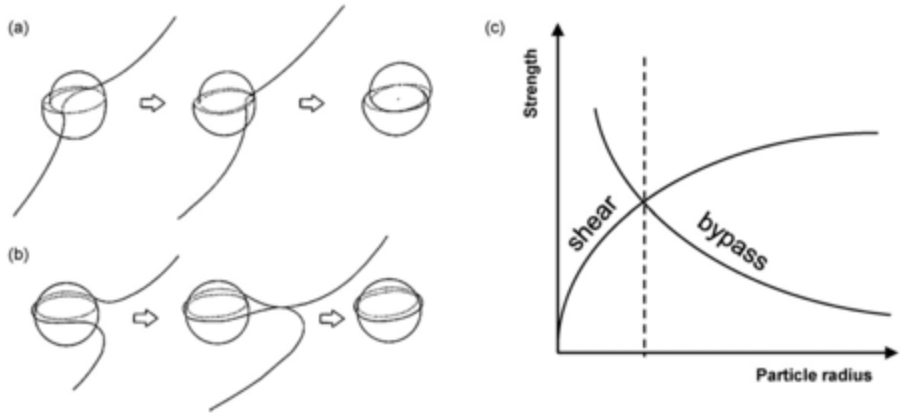

Figure 9: Dislocations motion around precipitates either by (a) Friedel or (b) Orowan mechanism (c) Relationship between precipitate radius and strength of the particles to resist shearing or bypassing by dislocations for a constant volume fraction of particles.[23]

2.6. Microstructural Characterisation

This work comprises different microstructural characterisations:

- Dilatometry
- Vickers micro-hardness testing
- SEM
- EDX mapping.

This section focuses on the principles of these characterisation to provide sufficient background information.

2.6.1. Vickers micro-hardness testing

The Vickers micro-hardness testing involves indenting the material with an indenter of certain geometry and material using small force over a small region. They are employed in situation where information about materials that have very fine microstructure, are multicomponent and or inhomogeneous [26]. The characteristics are enumerated below [27] :

- Indenter material: Diamond.
- Shape: Right pyramid with a square base (square pyramid) and an angle between the faces of 136°, outlined in Figure 10.
- Load applied: 0.01 – 10 N for 10-15 s
- Operation: The indenter is pushed into the material to the full load for 10-15 seconds. After removing the intender, the diagonals of the indentation are measured, and their average are calculated. The area of the sloping surface of indentation can be calculated, to yield the Vickers hardness.

$$HV = \frac{2F \sin\frac{136°}{2}}{d^2} \qquad (1)$$

$$HV \approx 1.854 \frac{F}{d^2} \qquad (2)$$

Where F is load in kgf and d is the arithmetic mean of the two diagonals of the indenter (d1 & d2) in mm and HV is the Vickers hardness.

Vickers hardness test has some advantages over other hardness measurement techniques:

- One type of indenter can be used for all types of metals and surface treatments.
- Precise under varying loads. If the material tested is homogenous and loads are above 200g, the Vickers values will be the same if tested regardless of the force.[27]

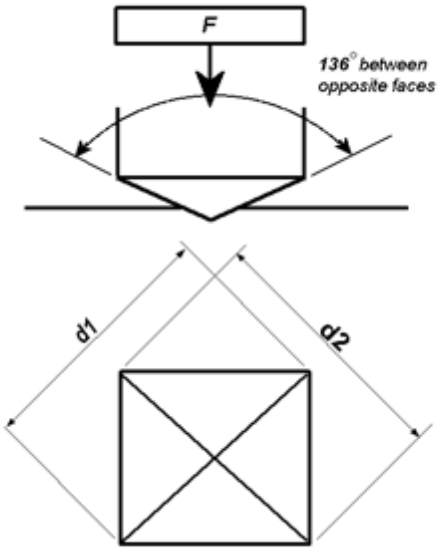

Figure 10: Vickers Hardness Testing: Indenter Geometry.[27]

2.6.2. Scanning Electron Microscopy (SEM) and Energy Dispersive X-ray (EDX) elemental mapping

SEM and EDX elemental mapping are employed for site specific characterisation of materials.

The main components of an electron microscope are electron sources, lens, lens aberration correctors, detectors and vacuum system. Different configurational signals of electron microscope yield different characteristic information. The different detectors can detect the backscattered electrons signal (BSEs), secondary electrons (SEs) and specimen current signal (SC). [28]

The BSEs are particular employed for compositional contrast, since BSEs are dependent on the atomic number of the sample surface and independent of beam energy. Figure 11 illustrates the relationship of backscatter coefficient with the atomic number. The backscatter coefficient is the ratio of BSEs to the total incident electrons. While SEs signals are employed for topological information.[28]

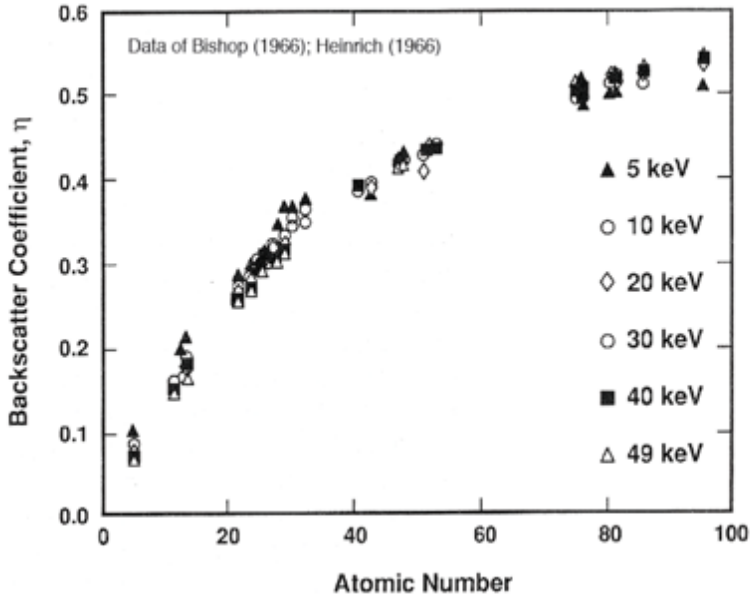

Figure 11: Backscattered electron yield increase with atomic number. [29]

EDX analysis employs the spectroscopy of X-rays generated by electron incidence and EDX elemental mapping electrons are scanned and analysed over a region. They are guided by SE detectors. The schematic of EDX elemental mapping is depicted in Figure 12.

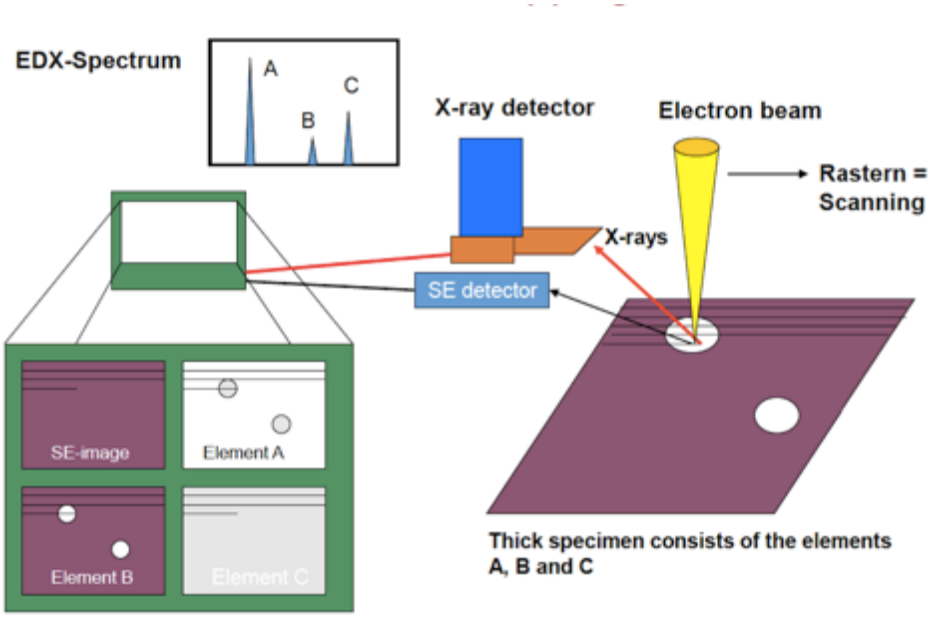

Figure 12: Schematic of EDX elemental mapping.[28]

2.6.3. Differential Scanning Calorimetry (DSC)

Differential Scanning Calorimetry (DSC) is a technique in which the difference in heat flow rate (or thermal energy) between a sample and reference is measured under a specific temperature program over the time.
The main components of DSC are shown in Figure 13 and they include:

- DSC sensors, crucibles and signal amplifier
- Furnace, temperature sensors and the atmosphere control
- Controller/Programmer
- Data Recorder

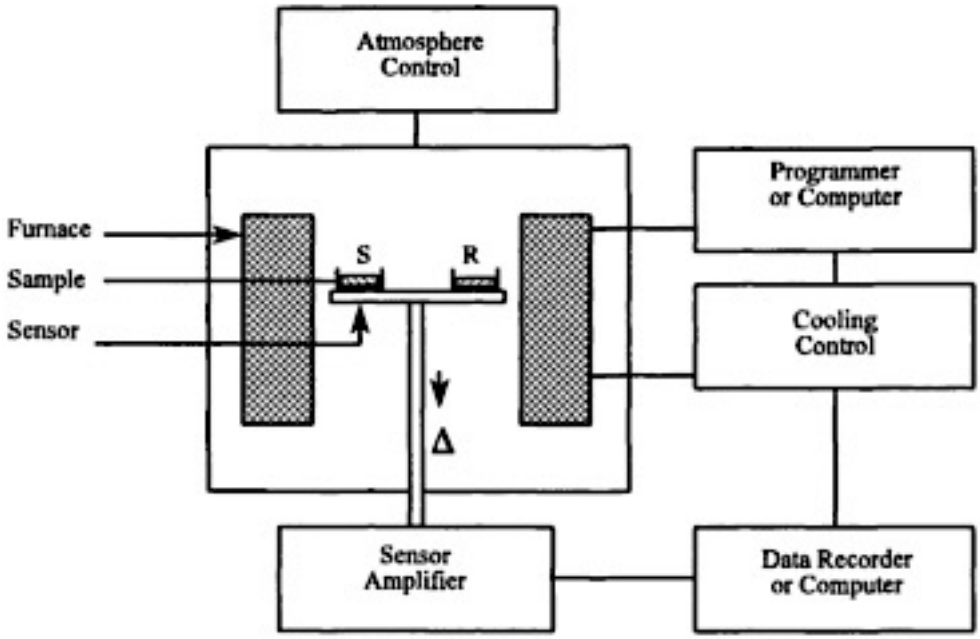

Figure 13: Schematic of components in DTA/DSC (Δ represents ΔT for DTA, ΔP for DSC). Taken from M.E. Brown.[30]

DSC is a standard technique employed to identify steps in precipitation sequence. Based on heat flow direction, the transformation can be classified as precipitation or dissolution (endothermic or exothermic reactions, respectively).[31]

2.6.4. Dilatometry

Dilatometry (DIL) is a technique in which the change in length over a temperature range is measured. The main components of DIL include (refer Figure 14) [30]:

- Pushrod, bearings and sample support.
- Furnace, temperature sensor and atmosphere control
- Displacement transducer
- Controller and Data Recorder.

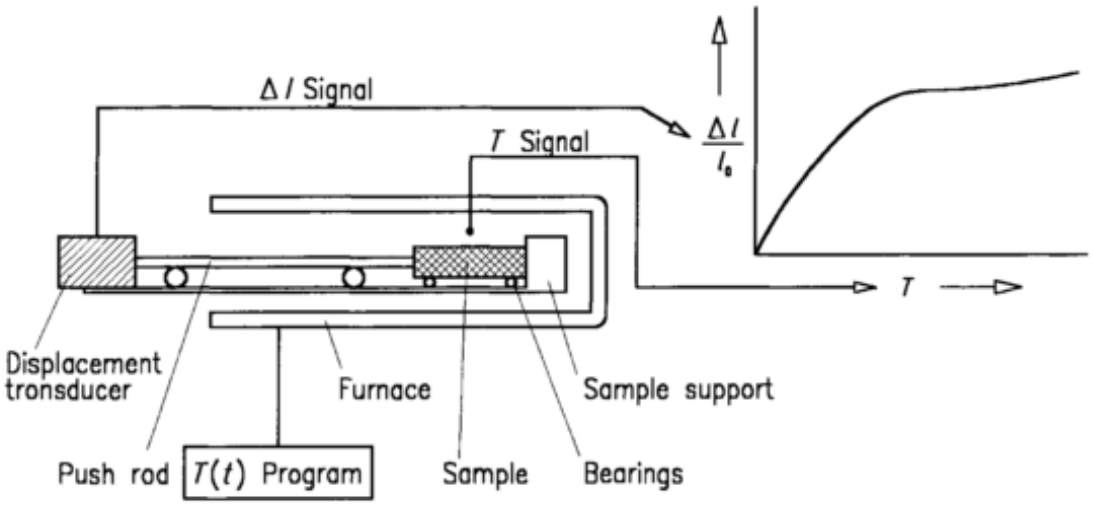

Figure 14: Schematic diagram of a dilatometer with its components. Taken from M.E. Brown..[30]

Dilatometry is a useful technique in the study of precipitation kinetics, particularly in phase changes associated with change in atomic volume. These changes are reflected in 1/3rd of linear change in length measured by dilatometry.[31]

2.6.5. Laser induced Ultrasound Spectroscopy testing (LUS)

LUS is a non-destructive materials characterisation technique that uses a pulsed laser to induce Surface Acoustic Waves (SAW). The Rayleigh wave velocity of SAW can be directly or indirectly used for materials characterisation or deriving material properties.

In LUS, a pulsed laser is focussed on the specimen, exciting SAW. They are detected by a continuous wave laser (CW) by beam deflection method. The main

components consist of a pulsed laser source, a cylindrical lens, the CW laser, a beam splitter lens and a detector. The schematic of the components is shown in the Figure 15.

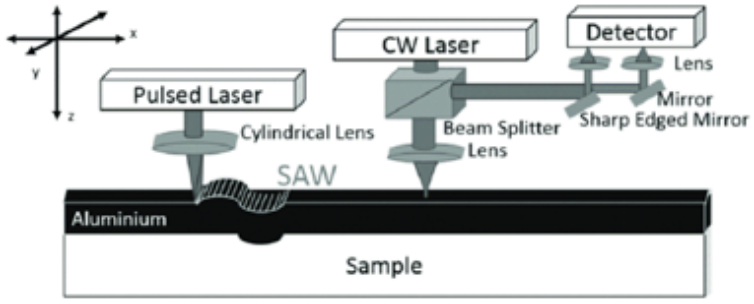

Figure 15: Schematic of LUS setup. Taken from [32].

3. Methodology

To understand the influence of the thermal treatment parameters, the alloy is heat treated under different aging temperatures, times and cooling rates and characterized by Vickers Micro-hardness Testing, Differential Scanning Calorimetry (DSC), Scanning Electron Microscopy (SEM) Energy Dispersive X-Ray (EDX) elemental mapping, Laser induced Ultrasound Spectroscopy (LUS) and Dilatometry.

The methodology is simplified into 5 processes: solution heat treatment, quenching, ageing, specimen preparation and characterisation.

1) Solution heat treatment: the material specimens are solution heat treated for 4h in furnace and 5 mins in the dilatometer.

2) After 1) the samples are quenched to room temperature at specific cooling rates.

3) Aging: the aging treatment depending on artificial and natural aging are done in the dilatometer and at room temperature, respectively.

4) Specimen Preparation: The surface of the specimens is prepared before the characterisation.

5) Characterisation: The specimens were characterized by different methods as stated above.

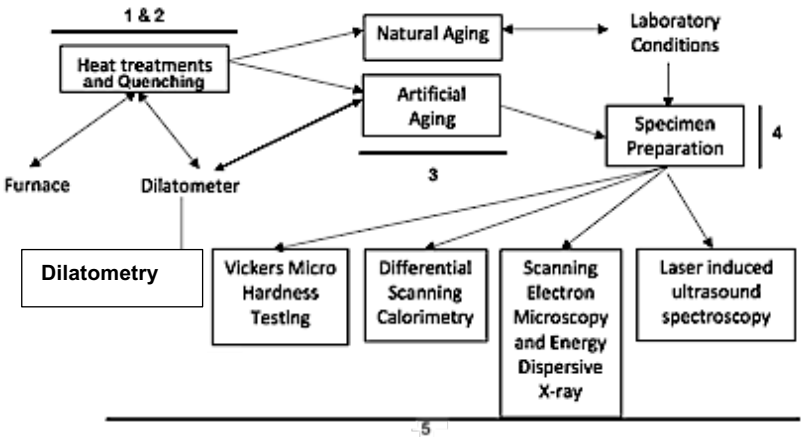

Figure 16:Schematic representing the experiments involving heat treatment, aging, specimen preparation and characterisation.

3.1. Material

The results of elemental analysis of the alloy AlSi7Cu0.5Mg is shown in Table 6.

Table 6: Elemental analysis of AlSi7Cu0.5Mg, obtained from Nemak Linz GmbH.

Element	Si	Fe	Cu	Mn	Mg	Ti	Al
(wt.-%)	6.83	0.107	0.531	0.0730	0.379	0.120	Balance

For the heat treatment and characterisations, specimens with dimensions listed in Table 7 were obtained.

Table 7: Characterisations and specimen dimensions and geometry.

Characterisation	Specimen dimension and geometry
Vickers micro-hardness testing	⌀4mmx8mm cylinder
SEM& EDX elemental mapping	⌀4mmx8mm cylinder
DSC	Ø 6mm x 1mm disc
LUS	40mmx15mmx4mm rectangular

3.2. Heat treatments in dilatometer and in-situ dilatometric measurements

The objectives of using the dilatometer for the experiments are two-fold:

1. To conduct under controlled parameters the heat treatments on the specimen over the whole parameter range.
2. To obtain in-situ linear dilatometric measurements.

The specimens were heat treated in the dilatometer after initial solid solution treatment in the furnace at 530°C for 4h. All the specimens are transferred on to the dilatometer, solid solution treated at 530°C for 5 mins and quenched at different cooling rates. In artificial aging experiments, the specimens were aged for different aging times and temperatures. In the natural aging experiments, they were aged at room temperature.

3.2.1. Artificial aging experiments

Artificial aging experiments were conducted over 3 different aging temperatures, 6 different aging times and 6 different cooling rates, which

results in a total number of 108 conditions. Figure 17 is showing the matrix of artificial aging experiments. Figure 18 depicts the temperature program of artificial aging experiments in the dilatometer.

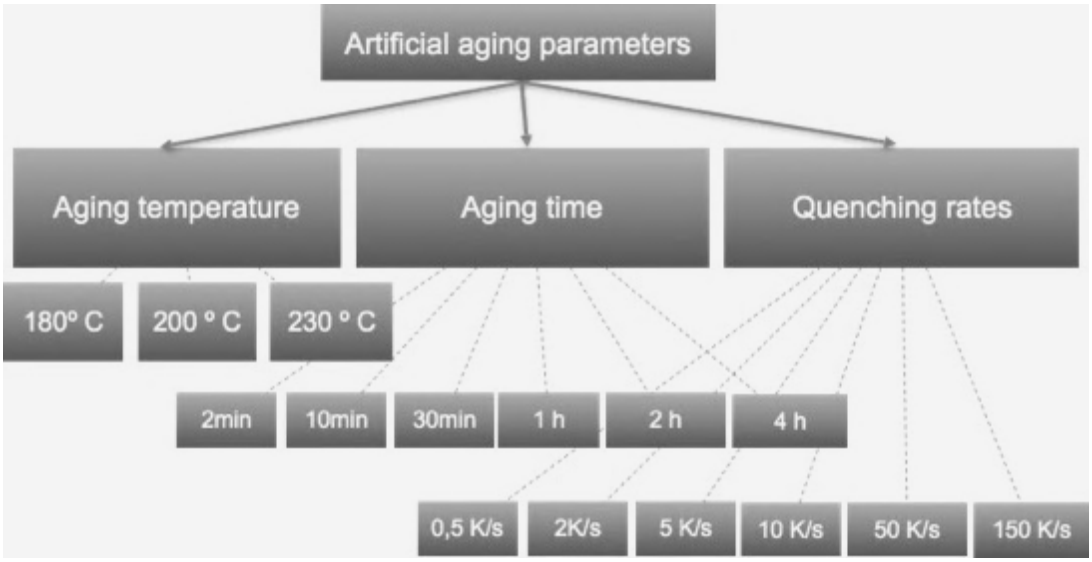

Figure 17: Artificial aging parameters and matrix of experiments.

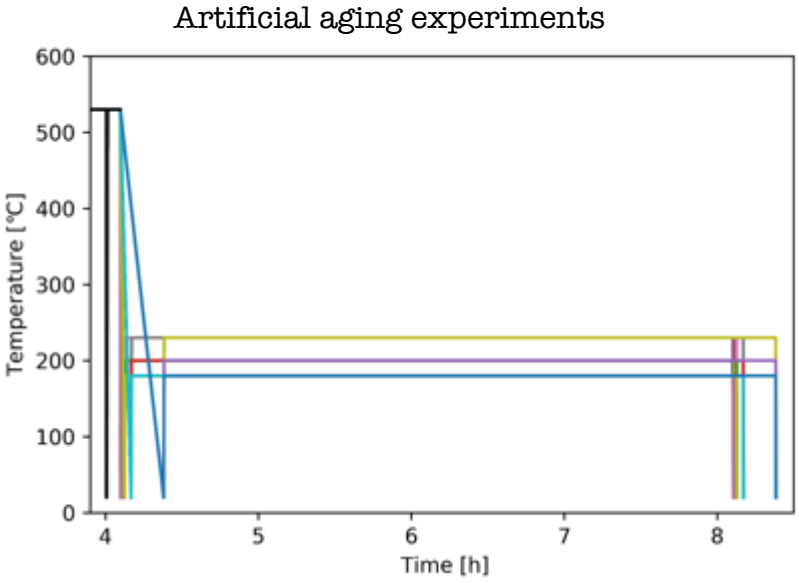

Figure 18: Temperature program of heat treatment for artificial aging experiments.

3.2.2. Natural aging experiments

Natural aging experiments were conducted over 11 different aging time and 5 different cooling rates. Typically, four hardness measurement were taken for

each aging time. Figure 19 is a schematic depicting the matrix of natural aging experiments. The Figure 20 shows the temperature program of natural aging experiments in the dilatometer.

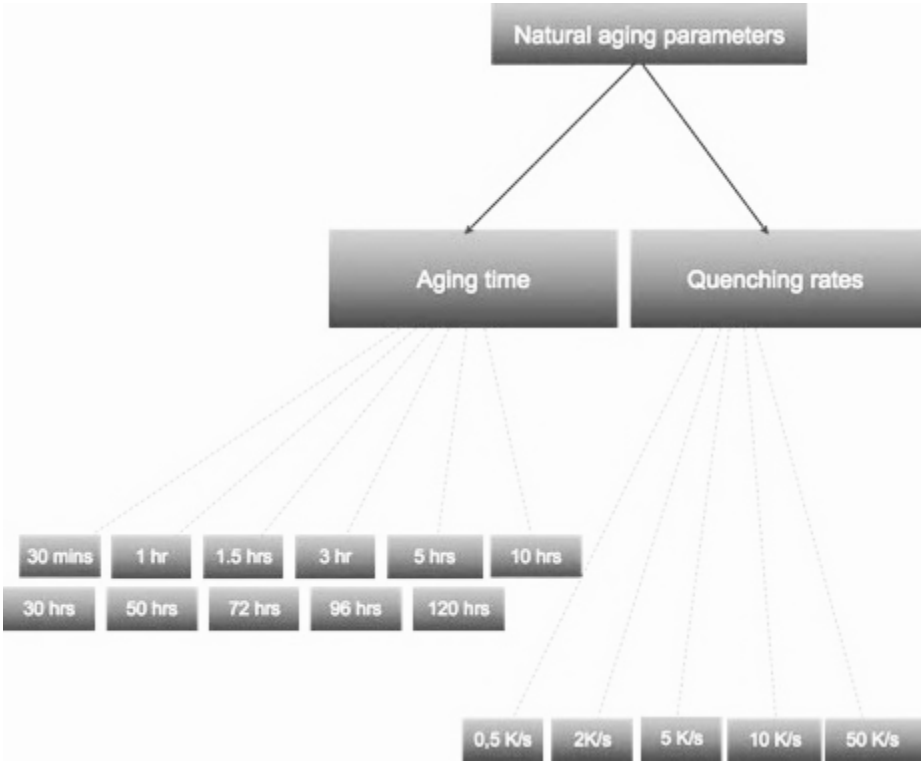

Figure 19: Natural aging parameters and matrix of experiments.

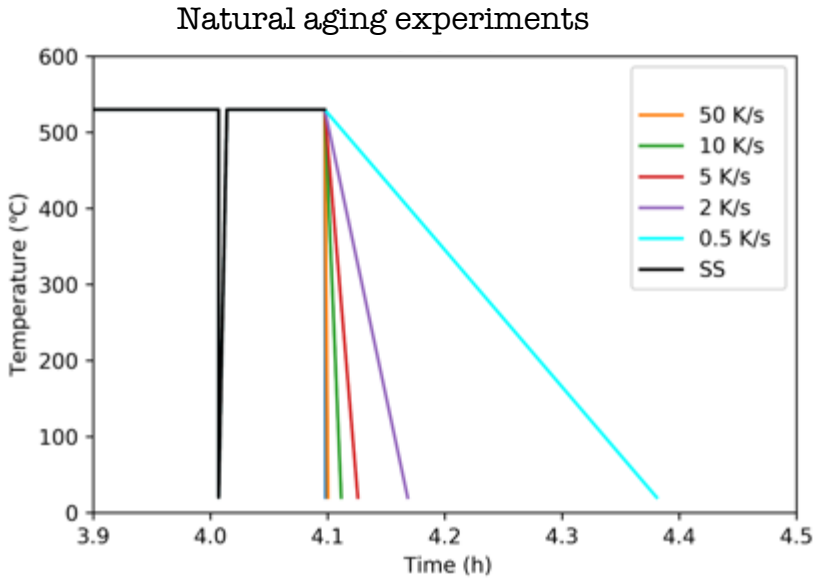

Figure 20: Temperature program of heat treatment for natural aging experiments.

3.2.3. Configurational information of the dilatometer

In this section, the configurational information of the heat treatment on the dilatometer Bähr 805 AD are described. Table 8 summarizes them in a tabular form.

Table 8: Configurational information of heat treatment on the dilatometer.

Temperature segment (°C)	**Time (s)**	**Programed heating rate (K/s)**	**Remarks**
20- 530	25.5	20	Inductive heating and under vacuum atmosphere (5 x 10^{-5} Pa)
530 [1]	300	-	Inductive heating for temperature correction b/w measured and programed, under vacuum atmosphere (5 x 10^{-5} Pa)
530- 20 [2]	3.4 - 1020	-0.5 to -150	Inductive heating for temperature correction b/w measured and programed and Ar/He quenched (430 L/h)
20– (180, 200, 230) [3]	8-11.5	20	Inductive heating
180, 200, 230 [3]	600-14400	-	Inductive heating for temperature

[1] Solid solution segment.
[2] Quenching segment.
[3] For artificial aging experiments.

			correction b/w measured and programed
(180, 200, 230) – 20 [3]	8-11.5	20	Ar/He quenched (430 L/h)

To optimize the quenching, they are done in segment with different configuration. Table 9 describes how the programmed cooling rates are achieved

Table 9: Configurations of quenching segment.

Temperature Segment(°C)	Quenching rate (K/s)	Settings of value 2 (430 L/h) of Bähr 805 AD
530- 80 80- 20	0.5	1% uncontrolled 25% uncontrolled
530- 200 200- 20	2	5% uncontrolled 100% uncontrolled
530- 160 160- 20	5	10% uncontrolled 100% uncontrolled
530- 110 110- 20	10	20% uncontrolled 100% uncontrolled
530- 20	50	100 % uncontrolled

The dilatometer records the experiment output parameters. For in-situ characterization of the artificial aging, the parameters: time, temperature, change in length and relative change in length are exported for further data treatment.

3.3. Specimen handling and preparation

After heat treatment, the specimens were stored in liquid nitrogen to prevent natural aging before the hardness measurements.

For the preparation of the specimen, a specimen holder was designed. Figure 21 shows the photograph of the specimen holder for the preparation. All the specimens were ground using SiC abrasives (P500, P1200, P2000, cutting fluid: water) and subsequently polished (3 µm, 1 µm, 0.05 µm OPS colloidal Si) and cleaned with ethanol before characterisation. The average time spend on specimen preparation is 30 mins. Therefore, all the measurements include 30 min of natural aging.

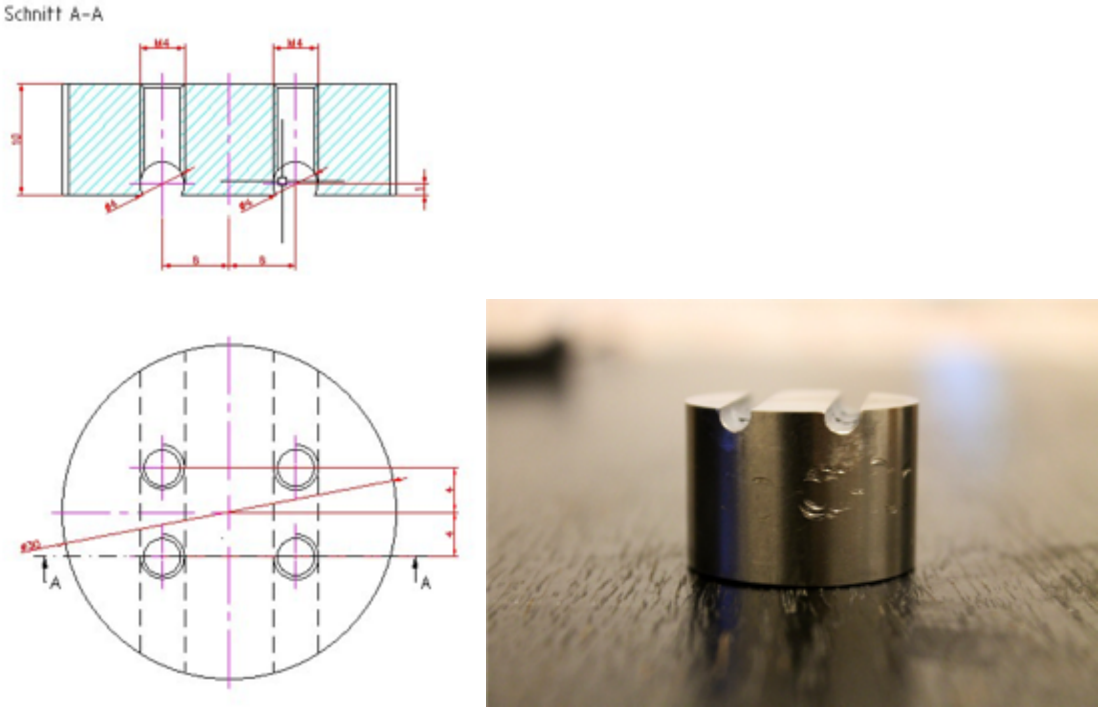

(a) (b)

Figure 21: (a) Engineering drawing and (b) photograph of the specimen holder for specimen preparation.

3.4. Vickers micro-hardness testing

Objective: To measure the micro-hardness as an indirect indicator of precipitation as function of quenching rate, aging time and temperature.

The hardness measurement was done on MHT4 Micro-Hardness Tester and the parameters are shown in Table 10.

Table 10:Parameters of Vickers micro-hardness measurements.

Force (N)	0.1
Holding time (s)	15
Slope (N/s)	0.03

The hardness indentations were optically guided into the Al-matrix using microscope of the MHT4 Micro-Hardness Tester. The hardness measurements were repeated 5 times for statistical results, and these indentations were typically spaced at least 90µm (6 times diagonal of indentations) from each other, to avoid strain hardening due to indentations.[33]

HV values were automatically calculated by formula (1). Exemplary images with HV values are obtained like the Figure 22.

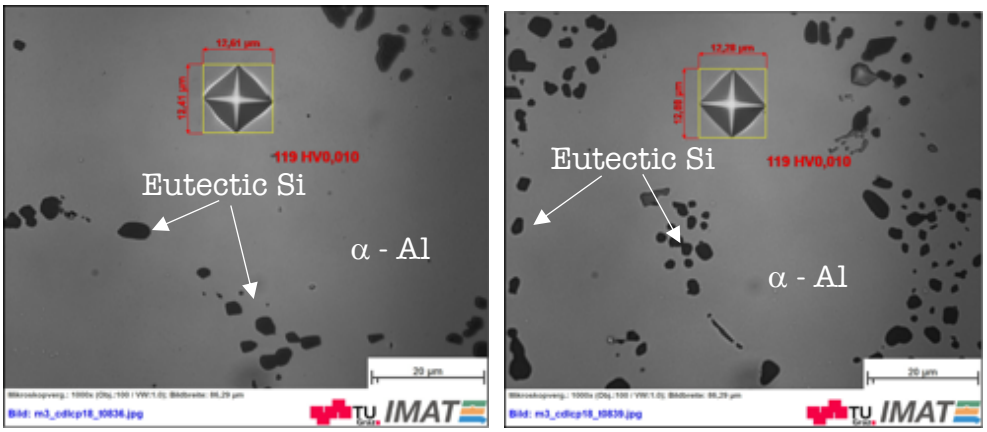

(a) (b)

Figure 22: (a), (b) Images of Vickers hardness indentations.

3.5. SEM and EDX elemental mapping

The objective of this investigations is to visualise large phases that can be resolved in a SEM and identify the elements.

Two samples of dimensions as shown in Table 7 quenched at 0.5 K/s and 50 K/s and aged at 230°C for 4h were investigated in the TESCAN Field Emission SEM The phases found were identified by EDX elemental mapping.
All the samples were coated with carbon adhesive tapes before investigation to improve the conductivity. Images were recorded using the SE detector and BSE detector in low energy. The beam energy was set at 5-10 kV. Images were captured across different magnification possible using SEM, to visualise phases that are at different scale.

3.6. DSC

The objective of DSC is to characterise the precipitation state of the heat-treated samples.

Discs of dimensions Ø 6mm x 1mm were used. They were heat treated in the dilatometer. The DSC experiments were conducted from 50 °C up to 500 ºC at a constant heating rate of 20 K/min and 40 K/min, using a Perkin Elmer DSC 8500.

The baselines for DSC results were constructed using Origin tools and the 99.5 % Al-reference heat flow curves. The DSC results were baseline subtracted. Samples were immediately stored in liquid nitrogen before testing.

3.7. LUS

The objective of LUS is to characterise aging by change in Rayleigh velocity of SAWs induced in the sample.

Two samples of dimensions as shown in Table 7: a solution heat treated (SHT) sample at 530°C for 4hours, aged at 180°C for 4hrs were characterized in the configuration as shown in the Figure 15.

The SAWs were excited at 11 positions. The time at which the SAWs pass the detector is obtained over distance travelled by SAWs. The distance travelled and time taken are plotted and linearly interpolated. The slope of this line estimates the Rayleigh velocity of the SAWs induced.

4. Results

In this chapter, the results of the characterisations are discussed and analysed keeping the objectives in mind. The chapter includes the Vickers hardness plot across the dependencies, SEM and EDX analysis, in-situ dilatometric curves and LUS characterisations.

The Figure 23 shows the Light Optical Microscopic (LOM) image of sample quenched at 10K/s after SHT. The images give a general idea of the distribution of eutectic silicon. The inter-dendritic distance remains the same. (dependent on the solidification of the cast).

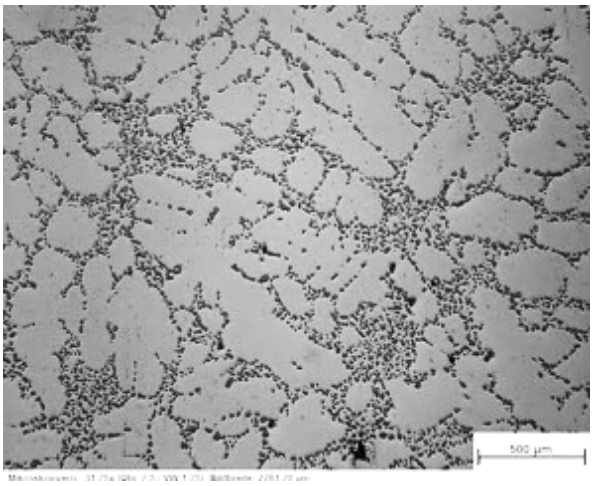

Figure 23: Light optical microscope (LOM) image of samples quenched at 10 K/s.

4.1. Vickers micro-hardness measurements

This section discusses the results of the Vickers micro-hardness test conducted on heat treated specimens. Based on the heat treatment, the section is classified into artificial and natural aging experiments.

4.1.1. Vickers micro-hardness measurements on artificially aged specimens

Micro-hardness test was conducted for heat treated specimens over the matrix of experiments as described in 3.2.1.

The aging curves were obtained by hardness measured across 108 different conditions. In this section they are depicted in 9 aging plots (Figure 24-28).

The hardness values appear to increase with increase in aging time up until peak hardness and decreases beyond it (Figure 25,27,29). The time required to peak hardness values decreases with increase in aging temperature (Figure 25,27,29).
The hardness value obtained at aging temperature 230°C are significantly lower than in the case of 180°C and 200°C (Figure 25,27,29).

The hardness values are particularly sensitive at low quenching rates (< 2 K/s) and less sensitive at higher quenching rates (Figure 26,28,30).

Holistic influence of aging temperature, time and quenching rate are represented by contour plots (Figure 30)

The error bars in the plot represent the standard deviation of each experiment (5 measurements). The average standard deviation across the measurements was found to be ±3.40 HV.

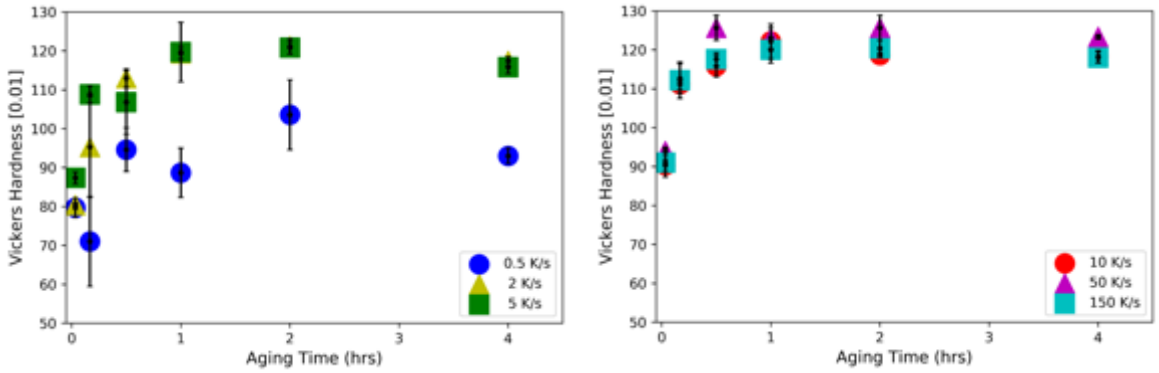

Figure 24: Aging curves for 180°C. (a) Quenching rates 0.5, 2,5 K/s (b) Quenching rates 10,50,150 K/s.

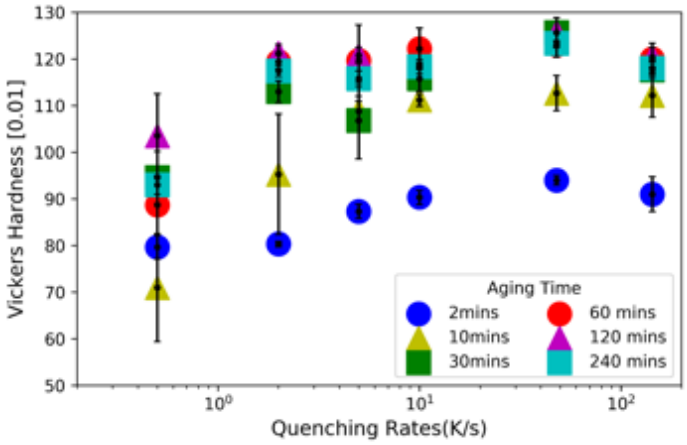

Figure 25: Effect of quenching rate at 180°C.

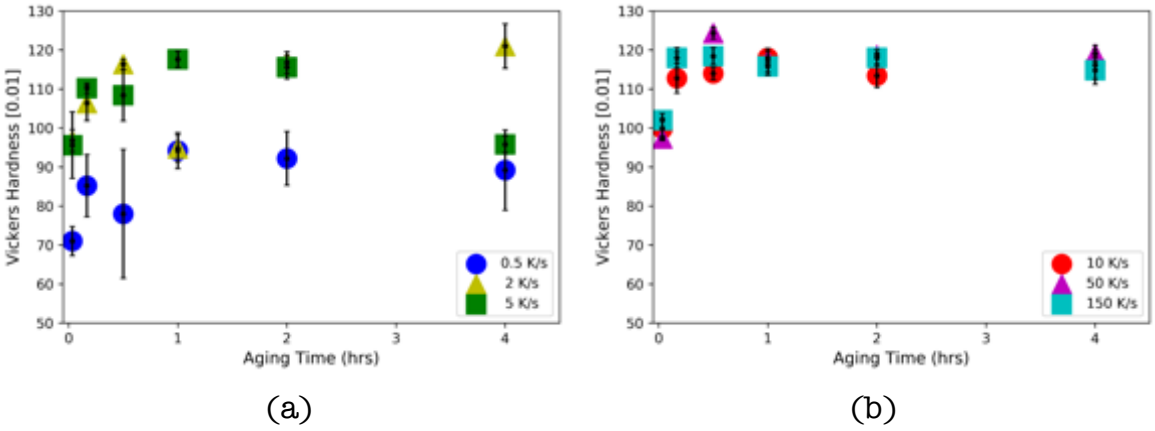

Figure 26: Aging curves for 200°C. (a) Quenching rates 0.5,2,5 K/s (b) Quenching rates 10,50,150 K/s.

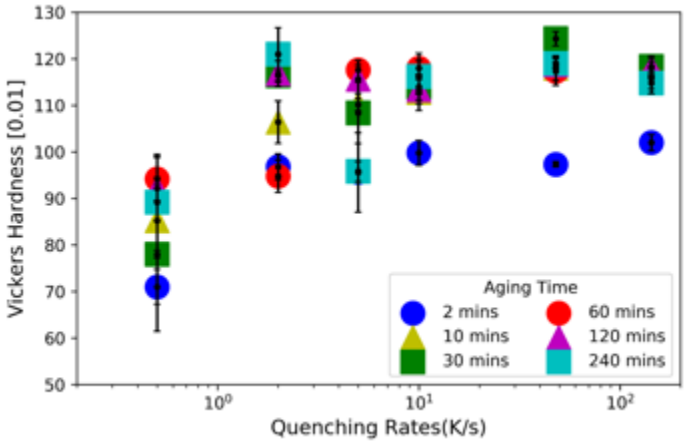

Figure 27: Effect of quenching rate at 200°C.

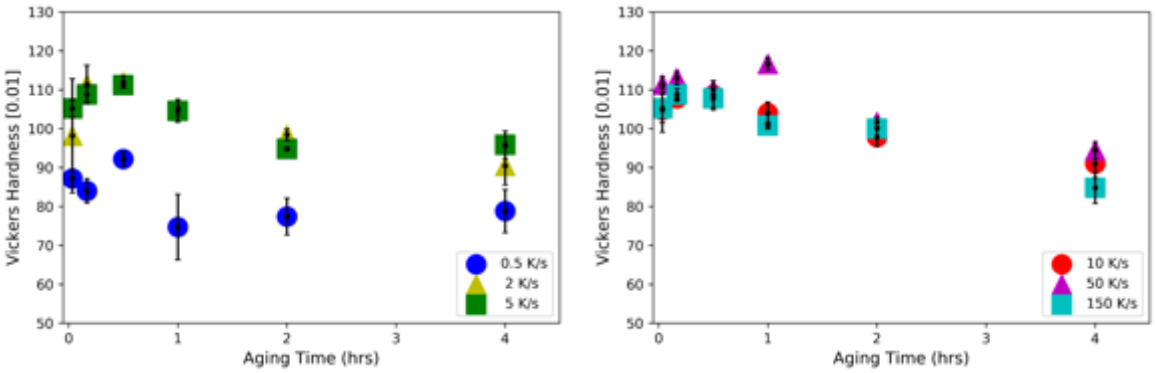

(a) (b)

Figure 28:Aging curves for 230°C.

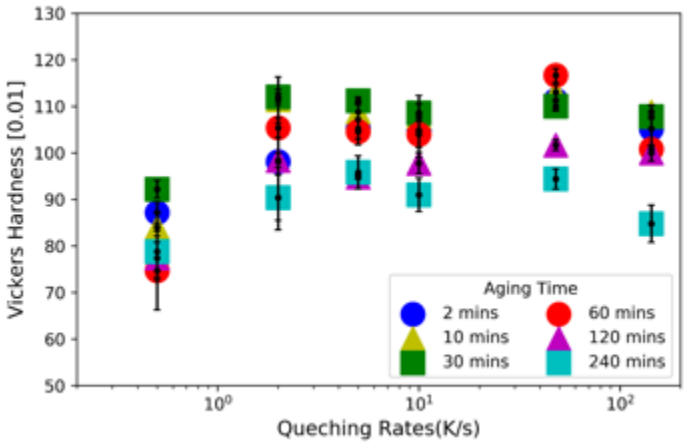

Figure 29:Effect of quenching rate at 230°C.

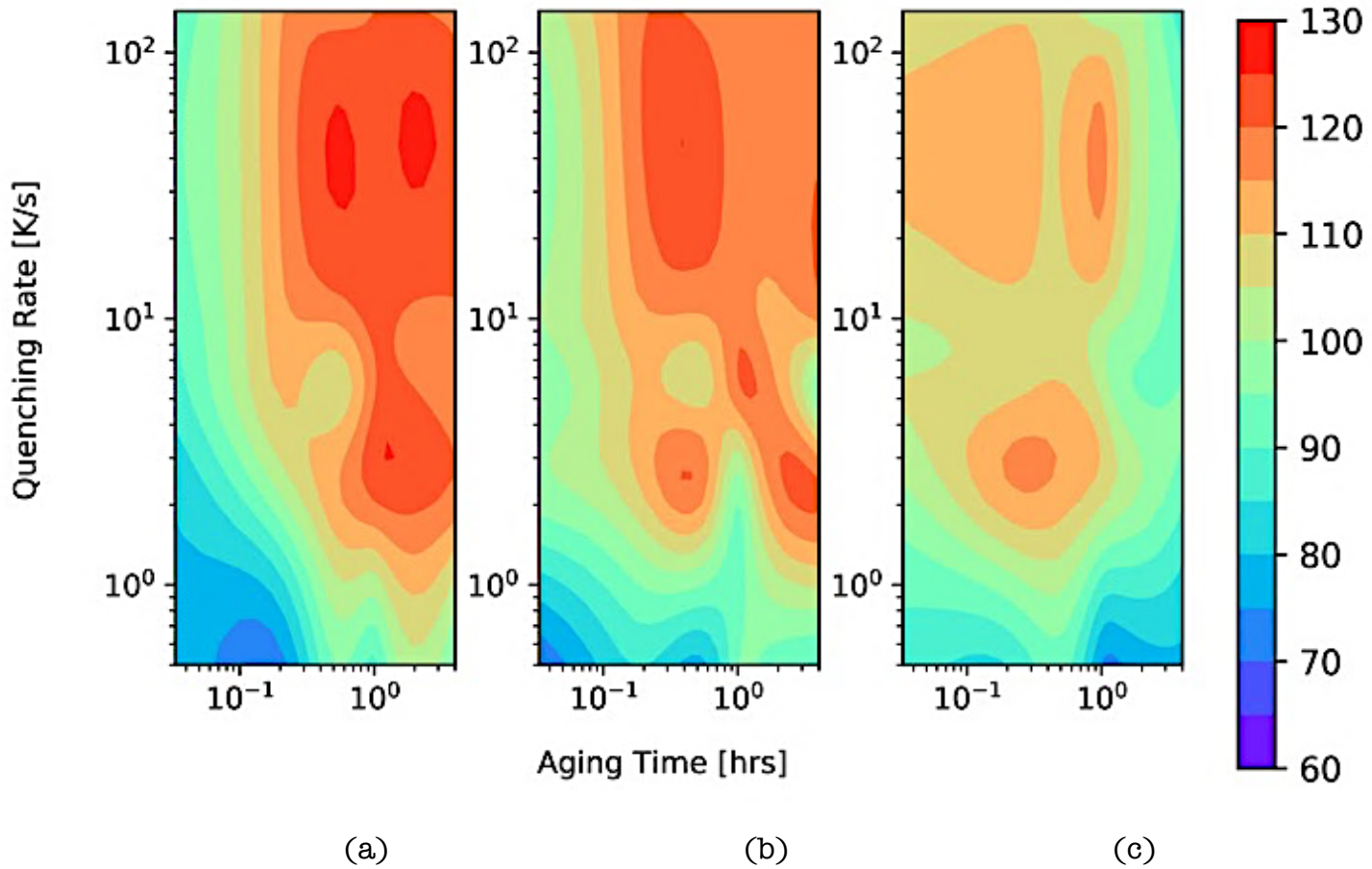

Figure 30: Contour plot of holistic influence of thermal treatment parameters for (a) 180°C, (b) 200°C, and (c) 230°C respectively. Colours mapped according to HV [0.01] values. Contour lines are drawn for 60-130 HV [0.01] with contour levels of 5 HV [0.01].

4.1.1. Vickers micro-hardness measurements on naturally aged specimens

Micro-hardness test was conducted for heat treated specimens over the matrix of experiments as described in 3.2.2.

The natural aging curves are represented in the Figure 31 and Figure 32. A gradual increase in hardness value is observed with increase in aging time. In the case of low quecning rates (0.5 K/s), there appears to be no significant increase in hardness value.

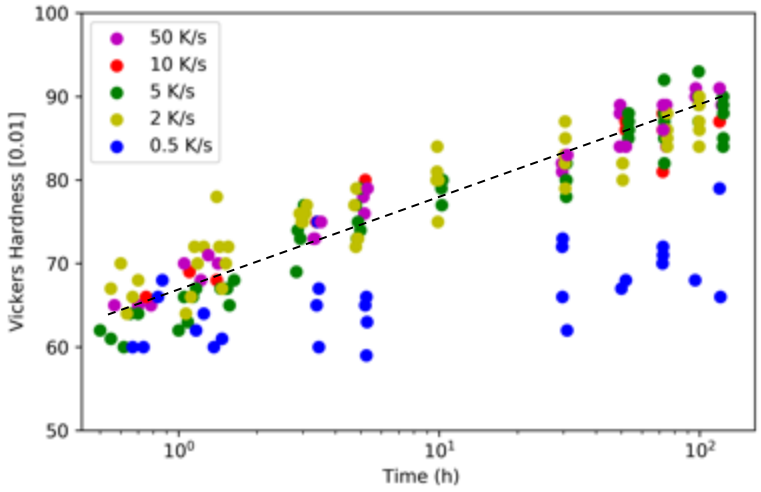

Figure 31: Vickers hardness as a function of natural aging time different quenching rates.

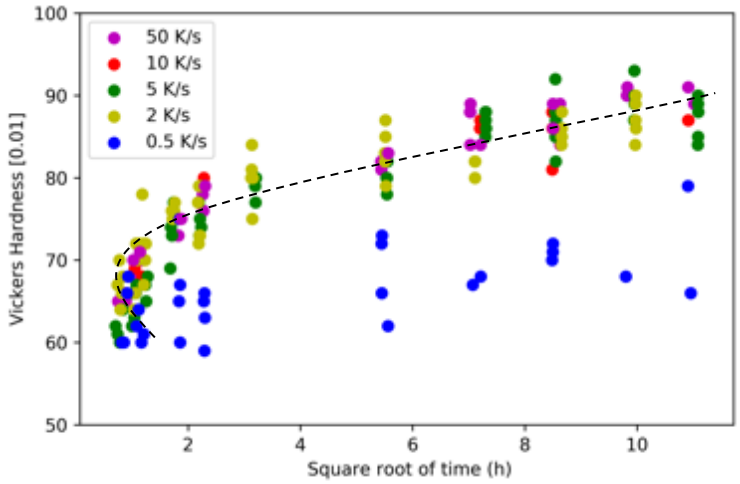

Figure 32: Vickers hardness as a function of square root of natural aging time different quenching rate.

4.2. SEM and EDX elemental mapping

The SEM analysis on sample that was quenched at 50 K/s and overaged at 230°C for 4 hours, revealed only the eutectic Si particles and Fe-intermetallic phases in Al matrix (Figure 33).
The SEM analysis reveal additionally to what was observed before, large and stable phases in the sample that was quenched at 0.5 K/s and overaged at 230°C for 4 hours. (Figure 34) These phases were identified as β and Q through EDX elemental mapping

Figure 35).

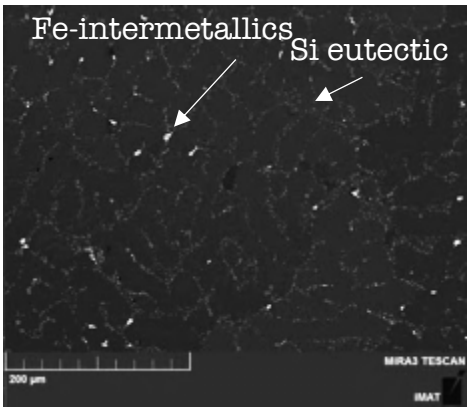

(a)

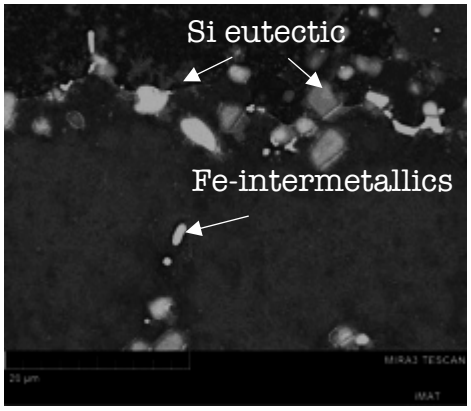

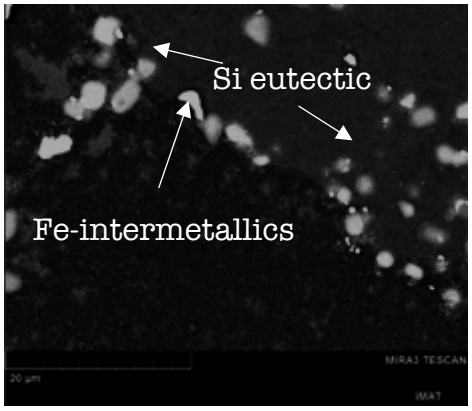

(b) (c)

Figure 33: BSEs image of specimen quenched at 50 K/s artificial aged at 230°C for 4hrs. Images (a), (b), (c) are of increasing magnifications respectively(indicated in the figure).

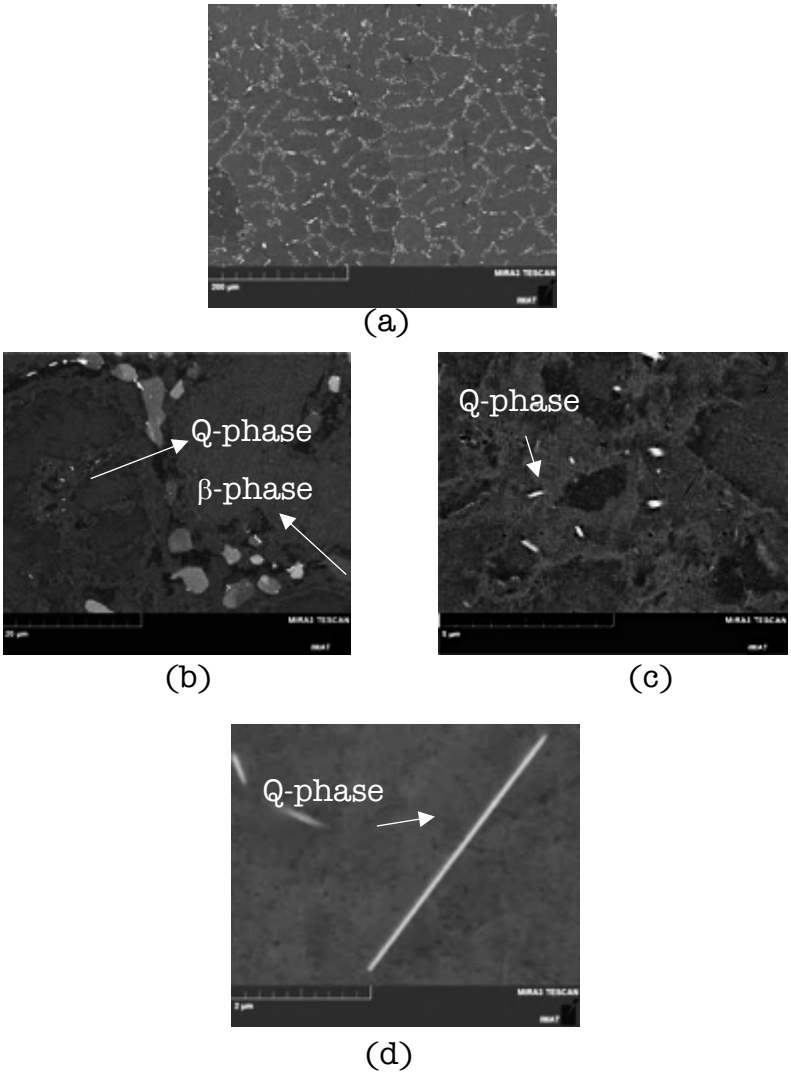

Figure 34: BSEs image of specimen quenched at 0.5 K/s artificial aged at 230°C for 4hrs. Images (a), (b), (c), (d) are of increasing magnifications respectively (indicated in the figure).

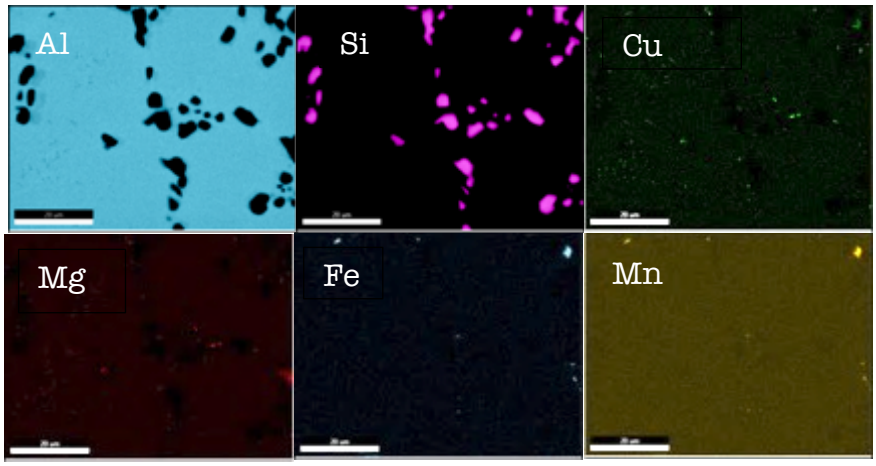

Figure 35: EDX elemental mapping of specimen quenched at 0.5 K/s artificial aged at 230°C for 4hrs.

4.3. In-situ dilatometric curves

The artificial aging treatment were conducted in the dilatometer. The instantaneous length measurement allows an in-situ characterisation of the alloy under heat treatment.

In this section, dilatometric curves for 3 different quenching rates (0.5 K/s, 5 K/s and 50 K/s), aged at 230°C are presented. The Figure 36 shows the relative change in length during aging (the relative change in length were normalised to zero at the beginning of artificial aging).

It could be stated that there was 0.031%, 0.065% and 0.081% of total increase in length for 0.5 K/s, 5 K/s and 50 K/s, respectively, aged at 230°C.

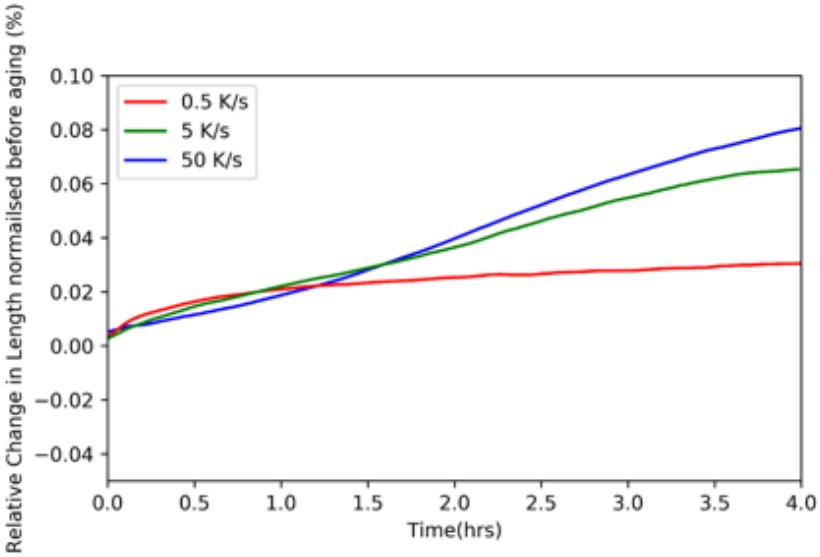

Figure 36: Dilatometric curves for artificial aging at 0.5,5 and 50 K/s at 230°C. Relative change in length during aging (Normalised to zero before aging) v/s Time.

Table 11: Results of in-situ dilatometric measurements for artificial aging at 230°C for (0.5,5,50) K/s

Quenching Rate	Relative length change after aging (%)
0.5 K/s	0.031%
5 K/s	0.065%
50 K/s	0.081%

After data treatment of in-situ dilatometric measurements, the differentiated and smoothed out curves on 1st order (a) and 2nd order (b) are depicted in Figure 37. It could be seen that there exists an acceleration of length change

during a time interval of 1-3.1 h of aging, depending on the quenching rate. The rate of the relative change in length reaches a local minimum at around 1.1h, 1.3 h and 1.6 h and a local maximum at around 2.8h, 2.8h and 3.1 h for 50 K/s, 5 K/s, 0.5 K/s quenching rates respectively. The acceleration peaks were found at around 1.9h, 2.0 h and 2.4 h for 50 K/s, 5 K/s and 0.5 K/s respectively.

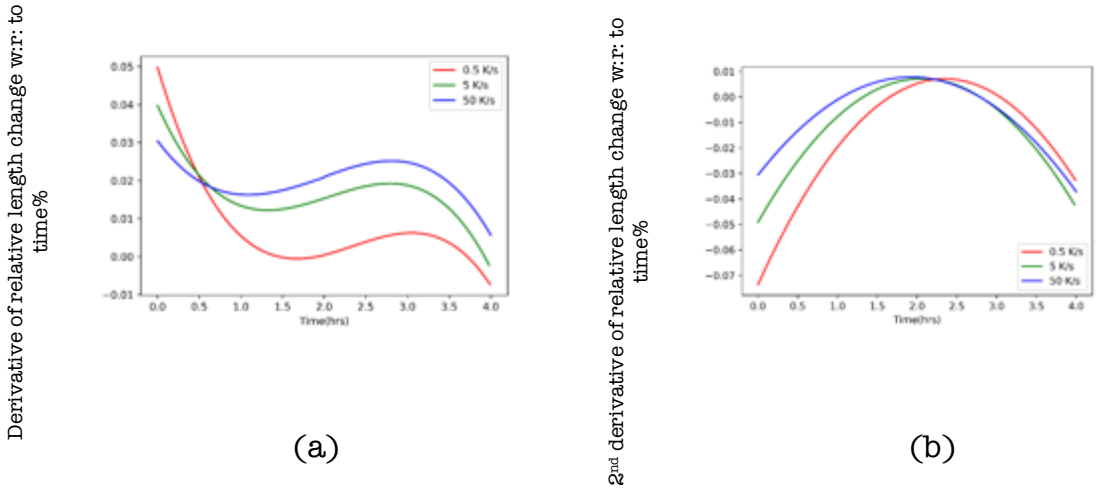

Figure 37: Derivative w: r: time dilatometric curves for artificial aging at (0.5,5,50) K/s at 230°C. Relative change in length during aging (Normalised to zero before aging) v/s Time.

4.4. DSC characterisation

The heat flow studies conducted for two samples after SHT and quenched at 0.5 and 20 K/s, are given below in Figure 38. They were baseline subtracted as described in the section 3.6.

From the DSC results the transitions peaks were identified. The transitions are described below: (for 40 K/min heating rate)

1) a broad exothermic peak under 150 ºC.
2) followed by a small endothermic peak.
3) two sharper peaks in the range of 200 ºC - 360 ºC.
4) an endothermic drift at temperature above 380 ºC.

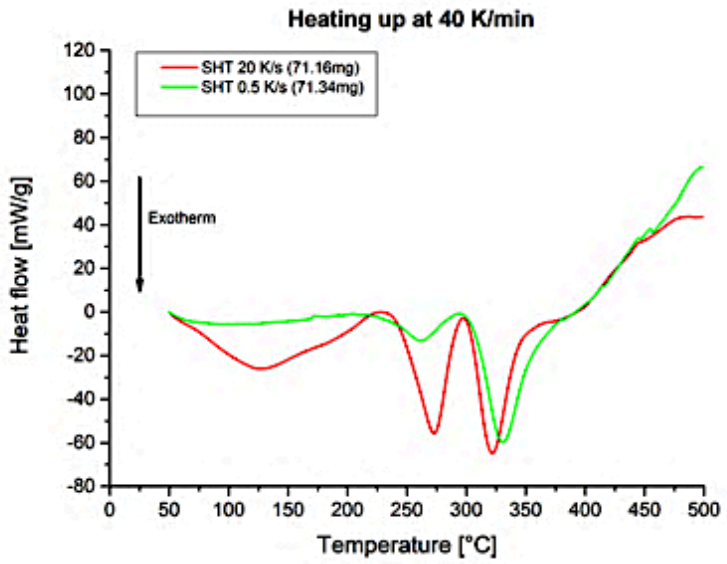

Figure 38:DSC baseline subtracted results. Mass of specimen indicated in brackets on the legends. Heating rate of 40 K/min.[34]

4.5. LUS characterisation

The results of the LUS characterisation is portrayed in Figure 39. The time taken for the SAWs to reach the detector were plotted as a function of distance travelled by them. The reciprocal of the slope of these curves gives the Rayleigh velocity of SAWs induced by the laser as 3016-3018 m/s.

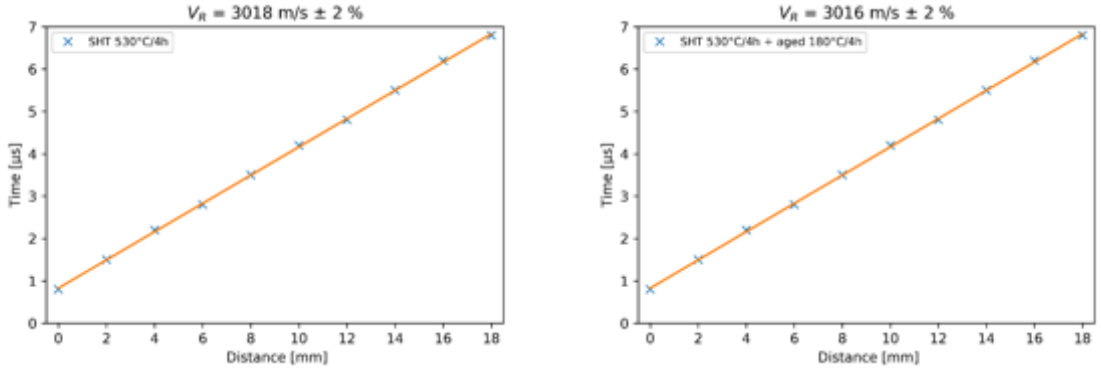

(a) (b)

Figure 39: LUS Characterisation. X-axis the distance travelled by SAW before detection and Y-axis time taken of detection. (a) Solution heat treated at 530°C for 4 hours (b) Solution heat treated 530°C for 4 hours and aged at 180°C for 4 hours.

From the above results, it could be stated there was no difference in rayleigh velocity of SAW induced between the two samples.

5. Discussions

In this chapter, influence of the thermal parameters is theorised with the help of relevant findings in experiment and in literature.

5.1. Precipitation kinetics

The transitions in the DSC results were identified as phase transformation using precipitation kinetics simulation in MatCalc by R. Wang [34] and literature [35]–[37].

The broad exothermic peak under 150 °C (1) was identified as the formation of θ'', β' and β''. The following endothermic peak (2) recognized as the dissolutions of metastable phases θ'' and β''. The first sharper peaks (3) is attributed to the formation of Q' & (4) for the formation stable precipitates Q and β. (5) are the dissolution of all these phases Q', Q and β.

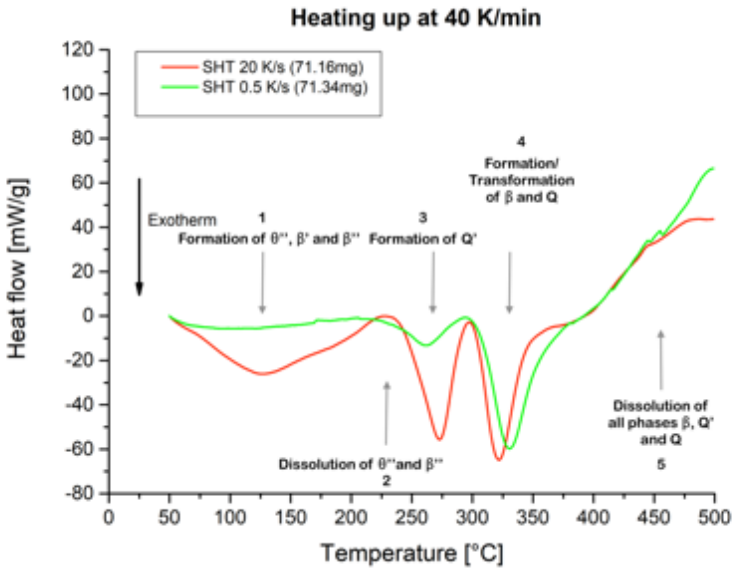

Figure 40: Interpreted DSC curves. Interpretations supported by MatCalc calculation by R. Wang. [34]

The dilatometric results reveal an overall increase in relative change in length with the aging time at 230°C. This is an evidence of secondary Si precipitates arising from the transformation of β''(Mg_6Si_5) to β'($Mg_{1.5}Si$) and subsequently to β(Mg_2Si). The excess Si are resulting from the stochiometric changes in these phases. The Si precipitates increase the average atomic volume of the unit cell of the Al-matrix.[31]

The Si precipitation start only after the G.P. Zones and β'' are dissolved [31]. The quenching rate influences the transformation of β'' -> β' + Si -> β + Si. More vacancies are created at high quenching rates, thus facilitating the Si precipitation [38]. Thus, for 50 K/s, a positive acceleration of length change is observed within a shorter time compared to 5 K/s and further shorter compared to 0.5 K/s. The transformations are kinetically hindered at more than 2.8h, 2.8 h and 3.1 h of aging time for 50 K/s, 5 K/s, 0.5 K/s respectively, with the depletion of the volume fraction of β'' and β'. Figure 41 depicts the (a) relative change in length (b) the rate of the relative change in length (c) the acceleration of relative change in length as a function of the aging time, with annotation of the various steps in Si precipitations.

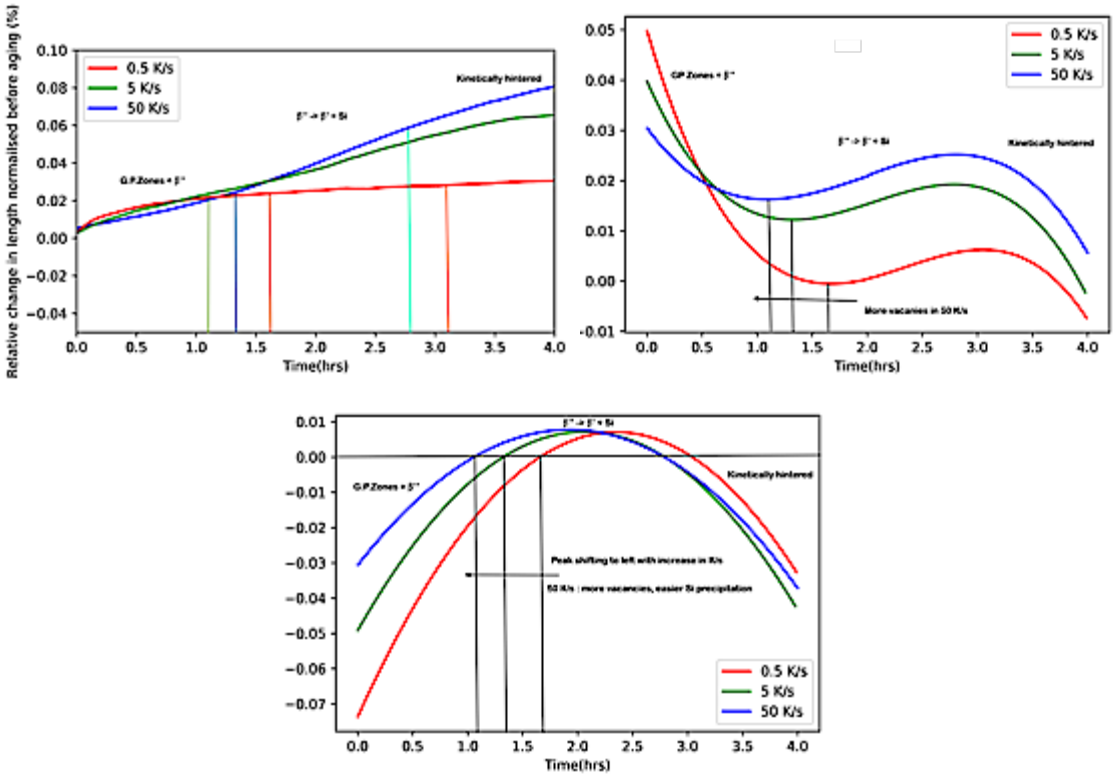

Figure 41: Dilatometric results for aging at 230 C for 4 h. (a) relative change in length v/s aging time (b) rate of relative change in length v/s aging time (c) acceleration of relative change in length v/s aging time.

5.2. Effect of aging temperature

- At higher aging temperatures, the peak hardness values obtained at shorter aging time.

With the increase in aging time, the hardness value increases up until peak hardness value and falls beyond it. The peak hardness value is faster in the case

of 230°C compared to the temperature 180°C and 200°C. Table 12 shows the time required for peak HV for different aging temperature.

Table 12: Approximate aging temperature and time for peak hardness value ranges for all quenching rates above 0.5 K/s.

	180°C	200°C	230°C
Peak HV obtained after aging time of	> 4h	~ 1h	< 1h

The precipitation proceeds through three stages: nucleation, growth and coarsening. Growth and coarsening are diffusion-controlled processes; thus, their temperature dependence can be explained. Higher temperatures would mean higher precipitation rates of the second phase atoms, so they reach critical radius for cutting to bowing transition faster.[39]

1) Similar effect was reported by P. Gumpl [16]. Figure 42 illustrates the aging curves and aging time for peak hardness reported.

Table 13:Aging temperature and time for peak hardness value, for quenching rate of 30 K/s by Gumpl. [16]

	180°C	200°C	230°C
Peak HV at	6h	1h	0.75h

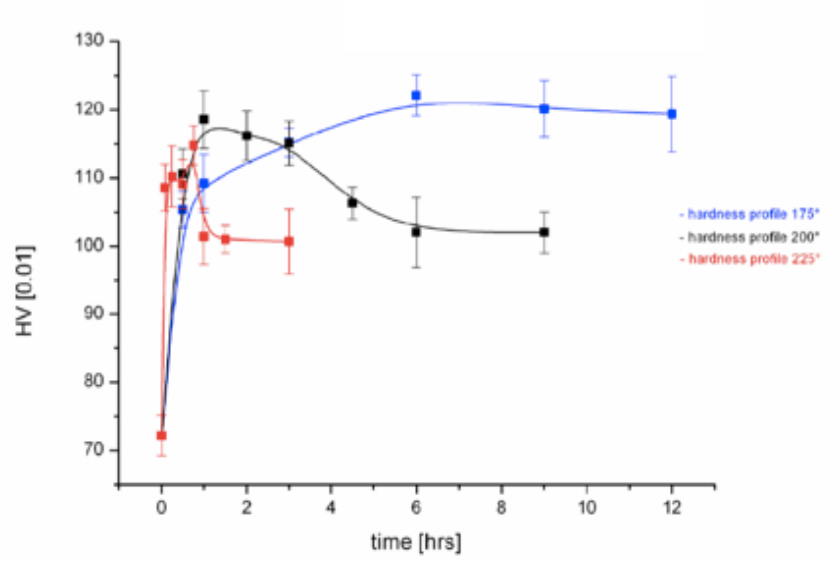

Figure 42: Vickers hardness profile of AlSi7MgCu0.5.[16].

2) Figure 43 shows MatCalc™ precipitation kinetics simulation results, by Krumphals et.al.[35]. Faster cutting to bowing transition, evident from decrease in yeild strength, when aged at 250°C compared to 200°C.

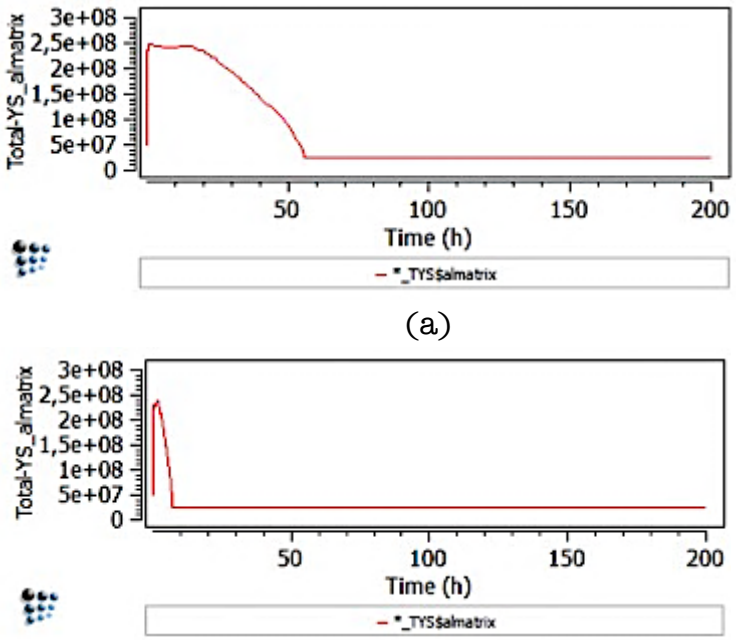

(a)

(b)

Figure 43: Evolution of yield strength in Pa against aging time at (a) 200°C & (b) 250°C, calculated by precipitation kinetics modelling software MatCalc™.[35]

- At higher aging temperatures (230 °C) the peak hardness values obtained are significantly lower.

There was 1 % and 7% decrease in average hardness values for aging temperatures 200°C and 230°C compared to 180 °C across all quenching rates and aging times. This could be accounted to be the faster coarsening of precipitates at 230°C. Peak hardness values for different quenching rates also found to be lower in the case of 230°C.

The significant drop in hardness in the case of 230°C could be due to transformation of coherent β'' to semi-coherent β'and incoherent β [36]. The contribution of β'' for hardening is higher than β'. This premise is supported by:

1) The DSC results show a small endothermic peak that onsets approximately at around 200°C. This peak was identified as dissolution of θ'' and β'', through precipitation kinetics calculations in MatCalc™.[34]

2) A decrease in phase fraction of β'' and an increase in β' was reported in TEM (Transmission Electron Microscopy) studies and MatCalc calculations by Krumphals et.al.[35]. Table 14 illustrates phases calculated by precipitation kinetics modelling software MatCalc™.

Table 14: Phases and volume fraction of phases calculated by precipitation kinetics modelling software MatCalc™.[35]

Aging Temperature/ aging time	200°C/1h	250°C/1h
Phases [vol.%], MatCalc	AlFeMnSi: 0.26 AlFeSi: 0.24 β'': 0.1 Q: 0.06	AlFeMnSi: 0.1 AlFeSi: 0.36 β''< 0.05 β' Q: 1.1

3) Dilatometry results reveal an overall increase in the length change of the specimen during aging. (Figure 36) This can be due to excess Si precipitates emanating due to transformation:

$$\beta''\text{- } Mg_6Si_5 \rightarrow \beta'\text{- } Mg_{1.5}Si \rightarrow \beta\text{- } Mg_2Si.$$

The Si precipitates have higher atomic volume (21.4 %) than in solid solution.

5.3. Effect of quenching rate

- At low quenching rates (< 2 K/s) the hardness values obtained are significantly lower.

A 16.55%, 27.93 % and 24.56 % decrease in average hardness value over all aging times in the case of 180°C, 200°C, 230°C aging temperatures respectively.

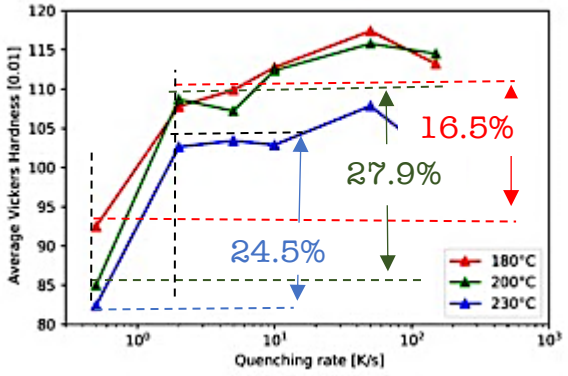

Figure 44: Average Vickers hardness over all aging time for different aging temperature.

In case of natural aging, similar effect can be seen. The hardness values do not increase significantly with time in the case of low quenching rates (Figure 31).

The reasons for the drop-in hardness at lower quenching rates must be the clustering of alloying elements, thus decreasing the supersaturation for the aging step. This proposition is supported by the following points:

1) Large and inhomogeneous phases were found on SEM image. This is an evidence for clustering of elements in quenching step and early stages of aging in the case of low quenching rates (< 2 K/s). (refer Figure 34)

2) Peak aging conditions are not reached in the case of low quenching rates, evident from aging curves. (Figure 30)

3) The decrease in super-saturation is evident from the DSC results (Figure 45). The area under the peak (2) (Figure 45) reveals the degree of supersaturation of solute in matrix before aging. Similar line of interpretation can also be found in [36].

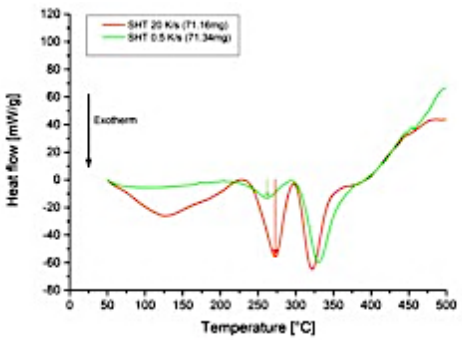

Figure 45: DSC curves indicating decreased super-saturation of the solute for lower quenching compared to higher ones.

In the case of SHT samples, the quenching rates determine the supersaturation of the solute in the matrix. The sample quenched at 0.5 K/s (green curve in Figure 45) , show a smaller peak (green arrow in Figure 45) indicating less driving force i.e., the supersaturation of solute for forming the metastable phase Q'. Conversely, in case of 20 K/s, there is a significant endothermic effect (red arrow in Figure 45).

4) The decrease in length change during isothermal aging (refer Figure 36), in case of 0.5 K/s relative to higher quenching rates 5 K/s and 50 K/s, indicates the lowering of super-saturation of solute.

$$\beta'' \rightarrow \beta' + Si \rightarrow \beta + Si.$$

The increase in relative change in length with aging time can attributed to transformation of metastable β'' to more stable β' and equilibrium phase β, which results in emitting secondary Si precipitations. The Si precipitates have a higher atomic volume, than when they are in solid solution.

If we assume that β''-> β' +Si starts at aging time of 0 hrs and is completed at 4hrs of aging for 50 K/s, we can look into the kinetics of this transformation. The lengths were normalised to 0.081% (max. length change in measurements) as 100%. Figure 46 shows the normalised fraction of the length change in % for 0.5K/s, 5K/s and 50 K/s. There was 37.57%, 80.37 % and 100% transformation after 4h of aging at 230°C, for 0.5 K/s, 5K/s and 50 K/s, respectively.

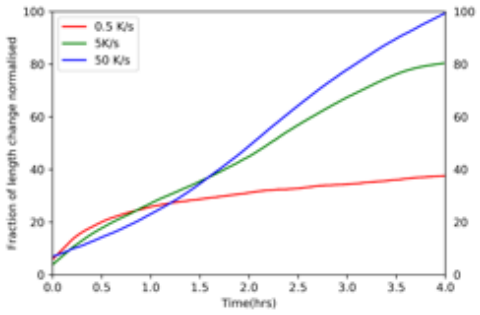

Figure 46: Dilatometric curves for artificial aging at 0.5,5 and 50 K/s at 230°C. Relative change in length during aging (Normalised to 0% before aging and 100% for 50 K/s maximum change) v/s Time.

The relatively slighter overall change in length in the case of lower quenching rates, can be explained by already formed stable phases, decreasing the potential of Si precipitations.

5) Similar effect was reported by Zhang.et.al. [36]. Figure 47 shows the yield strength as a function of quecching rate. A significant drop in yield strength at lower quenching rates can be seen.

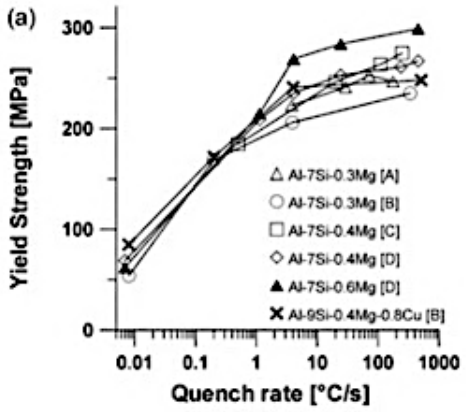

Figure 47: Quench sensitivity on yield strength of different Al-Si-Cu-Mg.[36]

5.4. LUS results

The LUS measurements were insensitive to artificial aging of the sample. The LUS measurement were conducted over macroscopic distances. The effect of precipitates on the velocity of SAWs could be negated by effects due to grain boundaries, Al-Si interfaces and other dislocations.

6. Summary and Conclusions

The results could be summarised into the following points:

- The Vickers micro-hardness numbers as a function of thermal treatment parameters: Quenching rate, aging time and temperature were portrayed.

- The hardness values increase to peak values with progression in aging time and decrease beyond it.

- With increase in aging temperature, the time required to reach the peak hardness value decrease.

- The lower hardness values obtained at higher temperature (230 °C) is due to coarsening of precipitates and transformations of coherent phases to stable and incoherent ones.

- Significant decrease in hardness value at lower quenching due to clustering during quenching, decreasing the aging potential for the precipitation hardening.

The relationship between the hardness value and thermal treatment parameters would enable to optimise the heat treatment according to the property and performance requirements.

It could be concluded that

1) The lower quenching rates are detrimental to the mechanical properties, but hardness values are less sensitive to quenching for rates above 2 K/s. This is of great industrial importance.

2) Dilatometry is an adequate tool for in-situ characterisation of specimens under isothermal heat treatments. They are one of the few tools that offer characterisation under isothermal conditions.

7. References

[1] I. J. Polmear, *Light alloys : from traditional alloys to nanocrystals*, 4th Editio. Elsevier/Butterworth-Heinemann, 2006.
[2] J. P. MONCHALIN *et al.*, *Laser-Ultrasonics for Materials Characterization*, vol. 7. 1992.
[3] M. Makhlouf and G. H., "The aluminum-silicon eutectic reaction: mechanisms and crystallography," *J. Light Met.*, vol. 1, no. 4, pp. 199–218, 2001.
[4] C. H. Caceres and J. R. Griffiths, "Damage by the cracking of silicon particles in an Al-7Si-0.4Mg casting alloy," *Acta Mater.*, vol. 44, no. 1, pp. 25–33, 1996.
[5] J. R. Davis, "Aluminum and Aluminum Alloys," *Light Met. Alloy.*, p. 66, 2001.
[6] M. Yildirim and D. Özyürek, "The effects of Mg amount on the microstructure and mechanical properties of Al-Si-Mg alloys," *Mater. Des.*, vol. 51, pp. 767–774, 2013.
[7] M. Zeren, E. Karakulak, and S. GÜmÜ, "Influence of Cu addition on microstructure and hardness of near-eutectic Al-Si-xCu-alloys," *Trans. Nonferrous Met. Soc. China (English Ed.*, vol. 21, no. 8, pp. 1698–1702, 2011.
[8] W. Reif, J. Dutkiewicz, R. Ciach, S. Yu, and J. Król, "Effect of ageing on the evolution of precipitates in AlSiCuMg alloys," *Mater. Sci. Eng. A*, vol. 234–236, pp. 165–168, 1997.
[9] Z. Ma, A. M. Samuel, F. H. Samuel, H. W. Doty, and S. Valtierra, "A study of tensile properties in Al-Si-Cu and Al-Si-Mg alloys: Effect of ??-iron intermetallics and porosity," *Mater. Sci. Eng. A*, vol. 490, no. 1–2, pp. 36–51, 2008.
[10] C. Puncreobutr, P. D. Lee, K. M. Kareh, T. Connolley, J. L. Fife, and A. B. Phillion, "Influence of Fe-rich intermetallics on solidification defects in Al-Si-Cu alloys," *Acta Mater.*, vol. 68, pp. 42–51, 2014.
[11] S. Ji, W. Yang, F. Gao, D. Watson, and Z. Fan, "Effect of iron on the microstructure and mechanical property of Al-Mg-Si-Mn and Al-Mg-Si diecast alloys," *Mater. Sci. Eng. A*, vol. 564, pp. 130–139, 2013.
[12] S. K. Shaha, F. Czerwinski, W. Kasprzak, J. Friedman, and D. L. Chen, "Effect of Mn and heat treatment on improvements in static strength and low-cycle fatigue life of an Al-Si-Cu-Mg alloy," *Mater. Sci. Eng. A*, vol. 657, pp. 441–452, 2016.
[13] T. Gao, K. Hu, L. Wang, B. Zhang, and X. Liu, "Morphological evolution and strengthening behavior of α-Al(Fe,Mn)Si in Al–6Si–2Fe–xMn alloys," *Results Phys.*, vol. 7, pp. 1051–1054, 2017.
[14] T. Sritharan and H. Li, "Influence of titanium to boron ratio on the ability to grain refine aluminium-silicon alloys," *J. Mater. Process. Technol.*, vol. 63, no. 1–3, pp. 585–589, 1997.
[15] E. Sjölander and S. Seifeddine, "The heat treatment of Al-Si-Cu-Mg casting alloys," *J. Mater. Process. Technol.*, vol. 210, no. 10, pp. 1249–1259, 2010.

[16] P. Gumpl, "Evolution of microstructure and microhardness during ageing of G-AlSi7MgCu0.5," Graz, 2011.
[17] G. a. Edwards, K. Stiller, G. L. Dunlop, and M. J. Couper, "The precipitation sequence in Al–Mg–Si alloys," *Acta Mater.*, vol. 46, no. 11, pp. 3893–3904, 1998.
[18] S. J. Andersen, C. D. Marioara, R. Vissers, A. Frøseth, and H. W. Zandbergen, "The structural relation between precipitates in Al-Mg-Si alloys, the Al-matrix and diamond silicon, with emphasis on the trigonal phase U1-MgAl2Si2," *Mater. Sci. Eng. A*, vol. 444, no. 1–2, pp. 157–169, 2007.
[19] S. P. Ringer, B. T. Sofyan, K. S. Prasad, and G. C. Quan, "Precipitation reactions in Al-4.0Cu-0.3Mg (wt.%) alloy," *Acta Mater.*, vol. 56, no. 9, pp. 2147–2160, 2008.
[20] K. Buchanan, K. Colas, J. Ribis, A. Lopez, and J. Garnier, "Analysis of the metastable precipitates in peak-hardness aged Al-Mg-Si(-Cu) alloys with differing Si contents," *Acta Mater.*, vol. 132, pp. 209–221, 2017.
[21] L. Ding, Z. Jia, Y. Weng, Y. Liu, S. Wu, and Q. Liu, "The morphology and orientation relationship variations of Q′ phase in Al-Mg-Si-Cu alloy," *Mater. Charact.*, vol. 118, pp. 279–283, 2016.
[22] A. Fabrizi, "The influence of Fe, Mn and Cr additions on the formation of iron-rich intermetallic phases in an Al-Si die-casting alloy," 2014, pp. 277–284.
[23] E. Sjölander and S. Seifeddine, "Optimisation of solution treatment of cast Al-Si-Cu alloys," *Mater. Des.*, vol. 31, no. SUPPL. 1, pp. S44–S49, 2010.
[24] E. Sjölander and S. Seifeddine, "Artificial ageing of Al-Si-Cu-Mg casting alloys," *Mater. Sci. Eng. A*, vol. 528, no. 24, pp. 7402–7409, 2011.
[25] R. Radis, "Numerical Simulation of the Precipitation Kinetics of Nitrides and Carbides in Microalloyed Steel," Graz University of Technology, 2010.
[26] "MICROHARDNESS TESTING." [Online]. Available: https://www.labtesting.com/services/materials-testing/metallurgical-testing/microhardness-testing/. [Accessed: 04-Feb-2019].
[27] "Vickers Hardness Test." [Online]. Available: http://www.gordonengland.co.uk/hardness/vickers.htm. [Accessed: 05-Jun-2018].
[28] H. M. Chan, "Lecture: 519.300 Materials Characterisation 2," 2016. [Online]. Available: https://online.tugraz.at/tug_online/LV_TX.wbDisplaySemplanDoc?pStpSplDsNr=12848. [Accessed: 31-Dec-2016].
[29] Goldstein et al, "Scanning Electron Microanalysis, Microscopy and X-ray," *Springer*, 2003.
[30] M. E. Brown, *Handbook of Thermal Analysis and Calorimetry, Volume 1 - Principles and Practice*. 1998.
[31] M. Kumar, C. Poletti, C. Collet, and H. P. Degischer, "Precipitation Kinetics in Age Hardening Al-alloys by Dilatometry and Differential Scanning Calorimetry," vol. c, no. Dil, pp. 1–6, 2010.
[32] E. Grünwald *et al.*, *Simulation of Acoustic Wave Propagation in*

Aluminium Coatings for Material Characterization, vol. 7. 2017.
[33] BS EN ISO 6507 - 1, "Metallic materials — Vickers hardness test — Part 1: Test method," *Br. Stand.*, 2005.
[34] W. René, unpublished manuscript, Graz University of Technology.
[35] M. Krumphals, F., Poletti, M. C., Lang, P., & Albu, "Optimisation and characterizastion of the microstructure and strength evolution of the alloy AlSi7MgCu0.5 according to different heat treatment and service condition.," in *LightMat 2013*, 2013.
[36] D. L. Zhang and L. Zheng, "The quench sensitivity of cast Al-7 Wt Pet Si-0.4 Wt pct Mg alloy," *Metall. Mater. Trans. A Phys. Metall. Mater. Sci.*, 1996.
[37] A. Assadiki, V. Esin, M. Bruno, and R. Martinez, "Stabilizing Effect of Alloying Elements on Metastable Phases in Cast Aluminum Alloys by CALPHAD Calculations," *Comput. Mater. Sci.*, 2018.
[38] F. Lasagni, A. Falahati, H. Mohammadian-Semnani, and H. P. Degischer, "Precipitation of Si revealed by dilatometry in Al-Si-Cu/Mg alloys," *Transl. Riecansky*, vol. 13309, pp. 1–6, 2008.
[39] D. G. Eskin, "Decomposition of supersaturated solid solutions in Al–Cu–Mg–Si alloys," *J. Mater. Sci.*, 2003.

8. List of figures

9. List of tables